Thrusts control the thermal maturity of accreted sediments.

Utsav Mannu[1,5], David Fernández-Blanco[2], Ayumu Miyakawa[3], Taras Gerya[4], and Masataka Kinoshita[5]

[1]Discipline of Earth Sciences, Indian Institute of Technology, Gandhinagar, India

[2] Barcelona Center of Subsurface Imaging, Institut de Ciències del Mar (ICM-CSIC), Barcelona, Spain;

[3]Geological Survey of Japan, AIST

[4]Institute of Geophysics, ETH Zurich

[5]Earthquake Research Institute, UTokyo

Correspondence to: Utsav Mannu (utsav.mannu@iitgn.ac.in)

Abstract.

Thermal maturity assessments of hydrocarbon-generation potential and thermal history rarely consider how upper-plate structures developing during subduction influence the trajectories of accreted sediments. Our thermomechanical models of subduction support that thrusts evolving under variable sedimentation rates and décollement strengths fundamentally influence the trajectory, temperature, and thermal maturity of accreting sediments. This is notably true for the frontal thrust, which pervasively partitions sediments along a low and a high maturity path. Our findings imply that interpretations of the distribution of thermal maturity cannot be detached from accounts of the length and frequency of thrusts and their controlling factors. Our approach takes these factors into consideration and provides a robust uncertainty estimate in maximum exposure temperatures as a function of vitrinite reflectance and burial depth. As a result, our models reduce former inconsistencies between predicted and factual thermal maturity distributions in accretionary wedges.

1. Introduction

Organic material transforms into coal, oil, and gas at rates primarily controlled by temperature. This transformation, critical for the hydrocarbon industry, is also useful to study the tectonic and sedimentary evolution of basins and orogens. The extent of this transformation in sediments, known as thermal maturity, can be measured as vitrinite reflectance, i.e., the percentage of incident light reflected from the surface of vitrinite particles in those sediments. Thermal maturity has been used to estimate the thermal evolution of igneous intrusions and seismic slip, the extent of low-grade metamorphism, porosity, and compaction in basin sediments, and the geothermal history of accreting material during subduction (e.g., Bostick and Pawlewicz, 1984; Rabinowitz et al., 2020; Fukuchi et al., 2017; Kamiya et al. 2017).

Inferences on the geothermal history of subduction margins based on thermal maturity depend on the trajectory followed by the accreting sediments (Miyakawa et al., 2019). Low-temperature, high-pressure metamorphic rocks in the subduction wedge are often attributed to the pressure maxima that typically predate the temperature maxima in accreted sediments undergoing diagenesis in the wedge (Ruh, 2020). However, the existence of complicated patterns in sediment trajectories is supported by numerical models and field observations (Giunchi & Ricard, 1999). As the orogenic wedge evolves, sediments accreting along different paths reach different depths and velocities and are exposed to different regional peak temperatures. Miyakawa et al. (2019) proposed to subdivide these trajectories based on their final characteristics, like thermal maturity. In this manner, the spatiotemporal evolution of sediments and their thermal maturity is regulated to a first order by the partition of incoming sediments along two endmember pathways; (I) a deeper path leading to elevated thermal maturities and constituted by underthrusted material, the ***high thermal-maturity path***, and (II) a shallower path that typically lies closer to the surface or gets frequently exhumed to near-surface levels, the ***low thermal-maturity path.***

Previous studies have used numerical and analogue approaches to study the trajectories of sedimentary particles, and their spatial and pressure-temperature evolution, as a function of changes in erosion, sedimentation, or décollement strength. The trajectory followed by underthrusted sedimentary units is primarily determined by orogenic wedge dynamics and its controlling forces (Plat, 1986). Although these sediments may only be exhumed near the backstop of the wedge, the trajectories of other accreted sediments generally deflect toward the surface under the influence of erosion (Konstantinovskaia and Malavieille, 2005). In fact, sedimentary particle trajectories gradually shift from deflection toward the surface near the front of accretion to final exhumation near the wedge backstop (Wenk and Huhn, 2013). Still, even under-thrusted sediments, which would co-relate to high-maturity paths in our study, have variable pressure-temperature paths (Ruh, 2020a). It is important to highlight that the majority of past studies have explored a snapshot of sediment trajectories, assuming that the general nature of trajectories remains relatively fixed with time or is stationary in nature. However, the intrinsic connection between thermal maturity and the comprehensive thermal exposure along the entire trajectory necessitates an in-depth investigation into the dynamic and transitory nature of sediment trajectories.

Although there is general consensus on the rate and extent of sediment trajectory transition from horizontal to vertical during accretion, the dynamic perturbations in sediment dynamics have yet to be adequately examined. For instance, while most studies show a great degree of correlation between the initial depth of incoming sediments and their final position in the wedge (e.g., Mulugeta and Koyi, 1992; Willett, 1992), a dynamic fluctuation in this correlation due to thrusting can result in non-stationary exhumation paths for accreting sediments in a wedge (e.g., Konstantinovskaia and Malavieille, 2005; Miyakawa et al., 2019). Much remains to be explored regarding the partition of high and low thermal maturity paths and how sediments travel inside natural wedges, given the conventional assumption that accreting sediments remain at the same relative depth and translate along the adjacent "layers" without vertical mixing throughout the tectonic evolution of the wedge (Hori and Sakaguchi, 2011).

Our assessment identifies a primary gap in existing research: the prediction and mapping of the initial sediment influx to their final location in the orogenic wedge. More specifically, the challenge lies in determining which portions of incoming sediment will predominantly constitute the core of the wedge and which will reside at comparatively shallower depths. Given that the maximum exposure temperature estimation from the thermal maturity is inherently reliant on the path of sediments inside the wedge, information on path diversity would inherently constrain the uncertainty in maximum exposure temperature used for the identification of paleothermal structures of subduction zones. Moreover, to better understand the time-depth paths of wedge sediments, their dependence on the initial state of undeformed sediments, and thus their thermal maturity, the factors that control the evolution of subduction-accretion systems, like sedimentation, erosion, and décollement strength, ought to be considered (Mannu et al., 2016; Simpson, 2010).

Here, we explore in detail the impact of accretion in a subduction wedge has on the thermal maturity of its sediments. We simulate subduction-accretion using 2D finite-difference thermomechanical models incorporating empirical thermal conductivity values from the Nankai accretionary margin. We track the evolution of thermal maturity by computing vitrinite reflectance (%R_o) on each marker and throughout the model, using three well-established methods of %R_o computation, as accretion develops the wedge under different sedimentation rates and décollement strengths. These factors notably alter the trajectories and thermal maturities of incoming sediments. Particularly, thrusts define sharp thermal maturity boundaries leading to stark differences in the thermal maturity of sediments that accrete in different thrust blocks, even when they follow similar trajectories and lay nearby.

2. Geological settings and model generalization

We use a generalized model for the subduction of an oceanic plate under a continental plate, with explicit integration of key parameters from the Nankai subduction margin off the Kii island in southwest Japan. The Nankai subduction margin is a product of the ongoing, northwest-directed subduction of the Philippine Sea Plate beneath the Amurian Plate at a convergence rate of 4.1-6.5 cm/yr (Seno et al., 1993; Miyazaki and Heki, 2001; DeMets et al., 2010). Past studies posit the initiation of this subduction within the Nankai region at circa 6 Ma (Kimura et al., 2014). The accretionary wedge adjacent to the Nankai margin is marked by the accretion of extensive sediment layers (>1 km), predominantly formed by overlying younger trench sediments atop Shikoku Basin sediments. Mean sedimentation rates of ~0.4 mm/yr for this area are calculated from sediment data onland and may largely reach the trench through submarine channels (Korup et al., 2014).

Another reason to select the Nankai subduction margin is that is it a particularly well-studied accretionary margin regarding its paleo-thermal history and thermal maturity distribution. For example, Underwood et al. (1993) and Sakaguchi (1999) used thermal maturity estimates from Shimanto accretionary wedge in the Nankai subduction margin to suggest that ridge subduction can explain the resulting paleo-heat flow. Following this, Ohmori (1997), published a distribution of thermal maturity and maximum exposure temperature for the Shimanto accretionary wedge identifying out-of-sequence activity in the region. The accretionary wedge adjacent to the Kumano forearc basin in the Nankai subduction margin has also been the subject of the NanTroSEIZE (Nankai Trough Seismogenic Zone) project, which drilled C0002 borehole during the 2012 Integrated Ocean Discovery Program Expedition 338. C0002 borehole is located approximately km southwest of Japan's Kii Peninsula in the Kumano Basin, within the Nankai accretionary margin, and extends 3,348 meters below the seafloor. Having data on both thermal maturity and thermal conductivity from the same borehole in subduction wedges is quite uncommon. To our knowledge, the C0002 borehole, located next to the Kumano forearc basin, is the only place where such data can be found in an accretionary wedge. Because of this unique characteristic, the C0002 borehole serves as an excellent dataset for validation purposes. We modify the thermal conductivity computation for sediments and décollement (see Table 1) to match the empirical relationship between depth and thermal conductivity, as measured on core samples in the borehole C0002 (Sugihara et al., 2014).

While these adjustments render our models somewhat specific to the Nankai accretionary wedge, we propose that the thermal conductivity values and trend are representative of patterns typically observed in forearc basins and accretionary wedges across the globe, making it broadly applicable to general subduction margins. For instance, in our simulations, the sediment thermal conductivity within our wedge steadily increases with depth from 0.96-4.0, which is within the range of thermal conductivity estimates for comparable depth in other subduction zones, such as the Hikurangi subduction margin, Japan Trench, and Taiwan subduction zone (Fig. S1, Henrys et al. 2003, Lin et al. 2014, Chi and Reed, 2008). As a result, we compare our simulation results not only to thermal maturity values in the Nankai accretionary margin but also to those of the Miura-Boso plate subduction margin in central Japan and the fold and thrust belts of the Western Foothills complex in western Taiwan.

3. Methods

We employ I2VIS, a conservative finite-difference 2-D thermomechanical subduction-accretion model with visco-plastic/brittle rheology (Gerya and Yuen, 2003a, 2003b). The code solves the governing equations for the conservation of mass, momentum, and heat as well as the advection equation with a non-diffusive marker-in-cell scheme constrained by thermal conductivity values inferred from Nankai accretionary wedge. Our numerical approach has several advantages over earlier attempts to simulate thermal maturity in an accretionary wedge, such as a more realistic geothermal profile, variable particle paths, and thermal evolution. In the following sections, we provide information regarding the governing equations, the modified thermal conductivity formulations based on the C0002 borehole, boundary conditions, the rheological model, model setup, surface processes, and the computation of thermal maturity.

3.1 Governing equations

The mass conservation is described by the continuity equation with the Boussinesq approximation of incompressibility.

$$\frac{\partial v_x}{\partial x} + \frac{\partial v_y}{\partial y} = 0 \qquad (eq. 1)$$

and the equation for conservation of momentum with an incompressibility assumption is expressed in the 2D-stokes equation, for the *x*-axis and *y*-axis, respectively,

$$\frac{\partial \sigma_{xx}}{\partial x} + \frac{\partial \sigma_{xy}}{\partial y} = \frac{\partial P}{\partial x} \qquad (eq. 2)$$

$$\frac{\partial \sigma_{yy}}{\partial y} + \frac{\partial \sigma_{xy}}{\partial x} = \frac{\partial P}{\partial x} - g\rho(T, P, C, M) \qquad (eq. 3)$$

Where density $\rho(T, P, C, M)$ depends on temperature (*T*), pressure (*P*), composition (*C*), and mineralogy (*M*).

The thermal equation used in the model is as follows:

$$\rho C_P \frac{DT}{Dt} = \frac{\partial q_x}{\partial x} + \frac{\partial q_y}{\partial y} + H_r + H_a + H_s + H_l \qquad (eq. 4)$$

where,

$$q_x = -k(T, C, Z)\frac{\partial T}{\partial x}, \quad q_y = -k(T, C, Z)\frac{\partial T}{\partial y} \qquad (eq. 5)$$

$$H_a = T\alpha \frac{DP}{Dt}, \; H_s = \sigma_{xx}\dot{\varepsilon}_{xx} + \sigma_{yy}\dot{\varepsilon}_{yy} + \sigma_{xx}\dot{\varepsilon}_{xy} \qquad (eq. 6)$$

Where $\frac{D}{DT}$ is the Lagrangian time derivative, and *x* and *y* denote the horizontal and vertical coordinates, respectively; σ_{xx}, σ_{xy}, σ_{yy} are components of the deviatoric stress tensor; $\dot{\varepsilon}_{xx}$, $\dot{\varepsilon}_{xy}$, $\dot{\varepsilon}_{yy}$ are components of the strain rate tensor; P is pressure; T is temperature; q_x, q_y are the components of heat flux in the horizontal and vertical direction; ρ is density; g is the vertical gravitational acceleration; C_P is the isobaric heat capacity; H_r, H_a, H_s, H_l, denote the radioactive, adiabatic, shear and latent heat production, respectively. $k(T, C, Z)$ is the thermal conductivity, a function of composition, depth, and temperature (Table 1).

In order to accurately assess thermal maturity, it is crucial to consider the temperature distribution, which necessitates a realistic thermal conductivity profile when modeling thermal maturity. Many geodynamic models assume that thermal conductivity decreases as temperature increases, following a defined relationship (e.g., Clauser and Huenges, 1995). These models typically predict a decrease in thermal conductivity with depth within accretionary wedges, as geothermal profiles tend to increase in temperature with depth. However, empirical data reveal a different trend: thermal conductivity increases with depth, primarily due to sediment porosity influencing shallow thermal conductivity (Henrys et al. 2003, Lin et al. 2014). Additionally, the thermal conductivity values calculated using the Clauser and Huenges model (1995) are significantly higher than those observed at shallow depths (< 3 km). To address these disparities, we incorporate the observed empirical relationship between depth and thermal conductivity from the IODP Site C0002 borehole in the Nankai accretionary wedge into our simulations. By adjusting the thermal conductivity formulation for sediments based on temperature and depth, we aim to replicate the empirical relationship observed in the core samples taken from the borehole at IODP Site C0002 (Sugihara et al., 2014) and account for the decrease in thermal conductivity near the surface caused by increased porosity. We modify the thermal conductivity formulation for sediments as a function of temperature and depth as follows.

$$k_{sed} = k_0 + \frac{807}{T + 77}\left(1 - \exp\left(\frac{-Z^2}{1.3e^7}\right)\right) \qquad (eq. 6)$$

$k_0 = 0.96\ and\ 1.5$ for the wedge sediment and décollement respectively. The larger thermal conductivity of the décollement emulates higher heat transfer in shear zones due to fluid advection (Fig. S1).

3.2 Rheological model

The expression for effective creep viscosities (η_{eff}) is computed as follows

$$\eta_{disl} = 0.5(\dot{\varepsilon_{II}})^{\frac{1}{n}-1} A_D^{\frac{1}{n}}\, h^m \exp\left(-\frac{E_a + V_a P}{nRT}\right) \qquad (eq.7)$$

$$\eta_{diff} = 0.5\frac{A_D}{S^{n-1}}\, \exp\left(-\frac{E_a + V_a P}{RT}\right) \qquad (eq.8)$$

$$\eta_{eff} = \left(\frac{1}{\eta_{disl}} + \frac{1}{\eta_{diff}}\right)^{-1} \qquad (eq.9)$$

where P is pressure (Pa), T is the temperature (K), R is the gas constant (8.314 J/K/mol), h is grain size (m) and, $A_D, n, m, E_a and\ V_a$ are experimentally determined rheological parameters: A_D is the material constant ($Pa^{-n}s^{-1}m^{-m}$), n is the stress exponent, m is the grain size exponent, E_a is activation energy (J/mol) , V_a is activation volume (J/Pa), and S is a stress factor for diffusion creep. As dislocation creep does not depend on grain size, therefore, we assume $h^m = 1 \cdot$ $\dot{\varepsilon_{II}}$ is the second invariant of strain tensor computed as

$$\dot{\varepsilon_{II}} = \sqrt{\frac{\dot{\varepsilon_{ij}} \cdot \dot{\varepsilon_{ij}}}{2}} \qquad (eq.10)$$

The model uses visco-plastic rheology to account for both brittle rheology of the shallower and colder rigid lithosphere and deeper, hotter ductile lithosphere and asthenosphere. Using the plastic yield threshold as per the Drucker-Prager criterion we limit effective viscosity as

$$\eta_{eff} \leq \frac{P.sin\varphi\,.(1-\lambda) + C.cos\varphi}{2\dot{\varepsilon_{II}}} \qquad (eq. 11)$$

Where c is cohesion and φ is an effective internal angle of friction or $\mu = \tan\varphi$ where is the coefficient of internal friction and λ the fluid pressure ratio.

3.3 Boundary conditions

A free-slip boundary condition is implemented on all boundaries, except on the lower boundary, which is passable in the vertical direction. Where we implement, an external free slip condition similar to where a free slip condition is satisfied at an external boundary such that

$$\frac{\partial V_x}{\partial x} = 0, and\ \frac{\partial V_y}{\partial y} = \frac{V_y}{\Delta Y_{external}} \qquad (eq. 10)$$

Where, $V_x\ and\ V_y$, are the velocities in the horizontal and vertical directions at the boundary, $\Delta Y_{external}$ is the depth that lies outside the modeling domain, and where free slip condition is maintained. Similarly, we set thermally insulating boundary conditions on all sides except the lower one where the external thermal boundary condition is implemented.

3.4. Surface processes

The rock-water/air boundary is simulated by an adaptive irregular grid that is advected horizontally and vertically and is coupled to the thermomechanical grid which controls the tectonic change of the surface. Apart from the tectonic changes, surface processes prescribed in the model can also change the topography. The surface process in the model is controlled by the conversion of rock markers to air/water and vice versa. All sedimentation in the model happens as a focused deposition of sediments from sea to land in morphological depressions (e.g., trench) is modelled as follows (Fig. S2)

$$Y_{new} = Y_{old} + K * Y_{fill} \qquad (eq. 11)$$

Where, $K = \min\left(\frac{V_{budget}}{V_{basin}}, 1\right)$

The shape of the basin and the resolution of the surface grid can lead to overfilling or underfilling when using the equation mentioned above to fill the basin. To address this issue, we calculate the volume of deposited sediments and adjust for any deficit or overfill in the subsequent step. This ensures that, over time, the total amount of sedimentation remains consistent with the prescribed value. However, it is challenging to ensure that all sediments added in a particular step are accommodated within the basins, especially in models with high sedimentation rates where significant runoff occurs. Therefore, the sedimentation rates mentioned in this study are computed as effective sedimentation rates after the model runs, rather than being predetermined. We perform multiple models runs (approximately 100) with sedimentation rates uniformly distributed in the range of 0.1-0.9 mm/yr. From these runs, we select models that exhibit appropriate sedimentation rates. This selection process ensures that the average sedimentation rates across all our models (ranging from 0.1-0.9 mm/yr) fall within the observed sedimentation rates in our chosen natural equivalent, the Nankai accretionary wedge in the southwestern subduction margin of Japan (Korup et al., 2014). For more specific information about the model run and prescribed sedimentary conditions, please refer to Table 2

3.5 Thermal maturity calculation

The model computes the $\%R_o$ of each marker to estimate the thermal maturity of sediments during the model run using three widely used methods of thermal maturity modelling Easy$\%R_o$ (Burnham and Sweeney, 1989, Sweeney and Burnham 1990), Simple%R_o (Suzuki et al., 1993) and Basin%R_o (Nielsen et al., 2017). All the models presented here employ a simplified parallel Arrhenius reaction model, which accommodates an array of activation energies for every component of the kerogen, allowing it to estimate thermal maturity under varying temporal and thermal scales. The Easy%R_o model by Sweeney and Burnham (1990) can be described using the following equations:

$$x_i(t) = x_{0i}\, exp\left(-\int A \exp\left(-\frac{E_{ai}}{RT(t)}\right) dt\right) \qquad (eq. 12)$$

$$X(t) = \sum_{i=1}^{N} x_i(t) \qquad eq. 13$$

$$F(t) = X(t=0) - X(t) \qquad (eq. 14)$$

$$\%R_o = \%R_{o0} \exp(3.7F) \qquad (eq. 15)$$

Where, x_{oi} are weights of reactions for ith component of the kerogen also described as the stoichiometric coefficient, A is the pre-exponential factor, E_{ai} is the activation energy of the ith component of the kerogen, R is the gas constant, T(t) is the temperature history, F is the amount of fixed carbon as a percentage and $\%R_{o0}$ is the vitrinite reflectance of the immature unaltered sediment. Sweeney and Burnham (1990) provided a set of 20 activation energies (E_{ai}) and the stoichiometric coefficient (x_{oi}) listed in Table 3. All thermal models used in this study use the same method of vitrinite reflectance computation albeit with different sets of activation energies, stoichiometric coefficient, pre-exponential factor and $\%R_{o0}$. Table 3 provides a comprehensive list of all these parameters.

All these approaches for computing %R_o yield similar trends albeit with different absolute values. In the interest of clarity, we have mostly illustrated Easy%R_o, which is the most extensively used method for Vitrinite Reflectance computation and hereafter we refer Easy$\%R_o$ as $\%R_o$, unless explicitly stated. $\%R_o$ is set to $\%R_{oo}$ in sediment markers at the start of the model till 2.5 Myr, while $\%R_o$ in markers for other rocks, air, and water is undefined at all times. After 2.5 Myr, the model computes $\%R_o$ on each marker as a function of temperature (T), time (t), and amount of fixed carbon as a percentage (F). The initial $\%R_o$ of newly deposited sediments is computed using an assumed water-sediment interaction temperature assumed to be the same as the thermocline. The thermocline used in the model has been estimated using the data obtained and made freely available by International Argo Program and the national programs that contribute to it for the region near Nankai (Fig. S3; https://argo.ucsd.edu, https://www.ocean-ops.org).

3.5 Model Set-up

The modelling domain is 3500 km wide and 350 km deep and is discretized into 3484 × 401 nodes populated with ~125 million markers (Fig. 1). The high resolution of 220 m (horizontal) × 130 m (vertical) that we assign at the site of accretionary wedge evolution, decreases steadily toward the edges of the modelling domain to a minimum resolution of 3000 m x 3200 m. The simulation consists of an oceanic plate converging with a velocity of ~5 cm/yr and subducting beneath a continental plate (Fig. 1). The oceanic plate consists of a 1-km-thick upper oceanic crust and a 7-km-thick lower crust. The thickness of the oceanic lithosphere depends on its age which is set to 20 Myr at the start of the simulation (Turcotte and Schubert, 2002). The initial age of the oceanic lithosphere corresponds to the age of the subducting lithosphere in the Nankai subduction margin (Zhao et al. 2021). Displacement along the megathrust, at the contact between subducting oceanic plate and the overriding continental plate, occurs in a relatively weak basal layer in accretionary wedges across the globe (Byrne and Fisher, 1990). We simulate this with a predefined configuration at the interplate, with a 350-meter-thick weak décollement below a sediment layer that is a km thick. The wedge forms above this interphase by the accretion of sediments against the continental plate. The continental plate consists of an upper and lower continental crust with thicknesses of ~20 km and ~15 km, respectively, and is underlain by a mantle lithosphere of ~25 km. We use a thin (10 km) "sticky air" layer to overlay the top face of the rock strata inside the model which is a fluid with a low viscosity of $5x10^{17}$ Pa·s, and a low density, similar to air (white in Fig. 1) or water (light blue in Fig. 1) (Crameri et al., 2012). The transition between the lithosphere and asthenosphere is prescribed to occur at 1300°C. A weak layer is emplaced at the junction of both plates, which fails mechanically and leads to subduction initiation. All sediments (light and dark brown in Fig. 1) are rheologically identical, but colours are alternated in time to allow tracking the development of different geological structures. Readers are referred to Table 1 for the rheological and thermal properties of all the materials used. Note that in our models, we refer to the measure all distances from the point where the continental and oceanic plates initially and is situated 1850 km from the right boundary of the modelling area. The terms "landward" and "seaward" indicate the relative direction towards the continental plate or the oceanic plate, respectively. The "Backstop" refers to the edge of the continental plate that buttresses the wedge and acts akin to an indenter for the accretionary wedge. The "forearc high" represents the highest point in the forearc zone, which includes both the accretionary wedge and the forearc basin.

3.6 Experimental Strategy

Here, we present a total of 10 models that vary in their effective basal friction or their effective sedimentation rate to discern patterns of thermal maturity evolution in wedge sediments. Models $M_0^{4.5} - M_0^{14.5}$ have no sedimentation and effective internal angle values for the décollement of φ_b= 4.5°, 7°, 9.5°,12° and 14.5° respectively. The chosen range of effective decollement strength is well within the range of values postulated by several studies for the Nankai accretionary wedge (Tesei et al., 2015). The rest of the models ($M_{0.1}^{9.5} - M_{0.9}^{9.5}$) and have a medium-strength décollement and variable effective sedimentation rate ranging from 0.1 to 0.9 mm/yr. In all the models presented in this study, sedimentation is limited to the trench, extending from the sea to the land. Restricting sedimentation to the trench allows us to observe and analyse the length and frequency of thrust sheets, enabling comprehensive investigation of their role in determining sediment trajectories. With these models, we evaluate the particle trajectory and $\%R_o$ of accreting sediments as a function of décollement strength and sedimentation rate. To restrict the number of parameters influencing our observations, models have no erosion. Moreover, all models lack surface processes during the first ~2.5 Myr and have sedimentation thereafter. Sediments used in the model have an angle of friction (φ) of 30° and a strain-softened value of 20° after a threshold of 0.5-1.5 strain. The coefficient of friction (tan φ) increases linearly between the strain thresholds.

4. Results

In our models, subduction begins at 0.1 Myr by failure of the weak material between continental and oceanic plate (Fig. 2, Fig. S4-S13 , also see supporting information movies). Continued and sustained accretion of sediments against the deforming continental crust forms the accretionary wedge from the interplate contact landwards. After ~5 Myr, all models develop a distinct wedge in agreement with the critical wedge theory (Davis et al., 1983). Surface slopes, measured by fitting a line in the surface of the wedge for every timestep between 2.5-7.5 Myr and reported as mean ± standard deviation, increase systematically, as effective basal friction increases from ~4.5° to ~14.5° (Fig. 1, Fig S4-S13, Table 2, $M_0^{4.5} - M_0^{14.5}$). Whereas models with a relatively weaker décollement, as ($M_0^{4.5}, \varphi_b$= 4.5°), have surface slopes of 0.95°± 0.3°, models with very strong décollement, as ($M_0^{14.5}, \varphi_b$= 14.5°), have slopes as steep as 5.9 ± 1° (Table 2). Our estimations of surface slopes consistently exhibit an excess of approximately 1.5° compared to the surface slopes predicted by the critical wedge theory (Table 2). This is probably due to the penetration of weaker decollement material into high shear zones, resulting in faults that are weaker than the strain-softened wedge material.

Models without trench sedimentation grow solely by accretion of incoming seafloor sediments, with frequent nucleation of frontal thrusts. Models with weaker décollements develop thrust sheets that are lengthier but remain active for shorter periods. This is clear when comparing, for models with increasingly strong décollement ($M_0^{4.5}, M_0^7, M_0^{9.5}, M_0^5, M_0^{14.5}$), the average distance between first and second frontal thrusts are 15.5 ± 7.0 km, 12.1 ± 3.6 km, 8.8 ± 3.3 km, 8.7 ± 2.1 km and 8.0 ± 1.8 km, respectively. Increasing sedimentation rate also leads to an increase in thrust sheet length from 7.3± 1.1 km for model $M_{0.1}^{9.5}$ to 13.8 ± 7.8 km in model $M_{0.9}^{9.5}$.

In models with similar basal friction, models with higher sedimentation rates have lengthier thrust sheets that remain active for longer periods (Table 2). Steeper surface slopes with increased décollement strengths and change in thrush sheet length with sedimentation and décollement strength are well-known effects that have been confirmed by previous numerical and analytical (Malavieille and Trullenque, 2009; Storti and Mcclay, 1995) models. All the reported values are mean ± Standard Deviation values recorded between 2.5-7.5 Myr in individual models. All models exhibit a temperature gradient that corresponds well with the temperature profile observed in the boreholes at IODP Site C0002 in the Kumano forearc basin, on top of the Nankai accretionary wedge (Fig. S14).

4.1 Thermal maturity of the wedge

Sediments are more thermally mature in wedges that have a higher sedimentation rate or décollement strength. For example, the mean %R_o of simulations for wedges with the highest sedimentation is 12% higher (0.75) than in those without sedimentation ($M_0^{4.5}$, Table 2, Fig. 3). Similarly, simulations of wedges with the strongest décollement have the highest mean %R_o (0.94) of all the simulations presented in this study.

Thermal maturity values increase with depth and landward distance from the trench to the forearc high irrespective of the decollement strength, sedimentation rates and method of thermal maturity computation (Fig. 3-4). The absolute value of %R_o and the rate at which thermal maturity values increase landward from the trench are larger for wedges with high décollement strength (Fig. 4A). For wedges characterized by the same décollement strength but higher trench sedimentation, we observe that the rate of thermal maturity increases in a landward direction from the trench and remains consistent across these wedges (Fig. 4B). Comparing the values of $\%R_o$ along a horizontal marker at the depth of trench in several models emphasizes this result; the model with the highest décollement strength reaches a maximum $\%R_o$ of 1.25 and has the highest rate of landward increase in thermal maturity (Fig. 4A). However, all models with similar décollement strength but different sedimentation do not visibly vary in their rate or magnitude of landward increase in thermal maturity. All models show a decrease in thermal maturity landward of the forearc high, commonly of 0.2 $\%R_o$. Other interesting observations that we explore below are the increased thermal maturity occurring in the vicinity of thrusts and the reversal in sediment maturity around out-of-sequence thrust active over longer times visible across several models (e.g. Fig. 3).

The magnitude of $\%R_o$ varies consistently among Easy$\%R_o$, Simple$\%R_o$ and Basin$\%R_o$. On average Easy$\%R_o$ have the smallest values, followed very closely by Basin$\%R_o$ (with an average difference of only 0.02). However, Simple$\%R_o$ had the highest average value of thermal maturity, being 0.16 and 0.13 higher than Easy$\%R_o$ and Basin$\%R_o$ (Fig. 3).

4.2 Sediment trajectory inside the wedge

In wedges with a higher décollement strength or sedimentation rate, sediments tend to follow high-maturity paths in larger proportions. We demonstrate this effect by creating a map of the thermal maturity of sediments at 7.5 Myr of the model run, mapped to their spatial position at 2.5 My of the model run to analyse the spatial correlation between sediment position (depth and distance) from the trench and thermal maturity (Fig. 5). We also show the mean thermal maturity attained by sediments at a given horizontal distance from the trench during this period by a dashed black line in Fig. 5. The scatter plot shows sharp changes in eventual thermal maturity with horizontal distance from the trench that relate to changes in sediment trajectory. The mean thermal maturity is also variable along the horizontal length of the wedge and has a periodicity (Λ) increasing in distance with higher sedimentation rate but relatively constant with changing basal friction (Fig. 5). The periodicity of mean %R_o was computed by finding the average wavelength of the auto-correlated mean %R_o. Whereas the mean thermal maturity has a short periodicity of ~7.2 km for the model $M_0^{9.5}$ with no sedimentation rates, the model $M_{0.9}^{9.5}$ shows the longest periodicity of 21 km. However, for all models with no sedimentation ($M_0^{4.5} - M_0^{14.5}$) , the periodicity remains relatively consistent between the range of 7-8 km.

Fig. 3 also represents the distribution of trajectories that exist in an accretionary wedge and how these trajectories get impacted under trench sedimentation (a subset of these trajectories can be viewed in the supplementary Fig. S15). Whereas in wedges with weak decollements ($M_0^{4.5}$), none of the shallowest half of incoming sediments reach %R_o > 1 in 5 Myr, 2% of sediments reach this value in wedges with strong décollement ($M_0^{14.5}$). The effects of décollement strength in the thermal maturity of sediments can be quantified as well at deeper levels, with one-eighth vs more than half of the sediments surpassing values of %R_o = 1 for the deepest half of incoming sediments (12% and 54% respectively) in weak vs strong-decollement wedges ($M_0^{4.5} vs\ M_0^{14.5}$), respectively. In wedges for the model without sedimentation ($M_0^{9.5}$), the top half of the incoming sediments fail to achieve %R_o > 1, as opposed to ~ 15% of them reaching %R_o > 1 in the models with a sedimentation rate of 0.9 mm/yr ($M_{0.9}^{9.5}$). In sum, the proportion of sediments in the top half and bottom half of the wedge that reach high maturity steadily increases with both sedimentation rate and décollement strength (Table 2).

4.3 Patterns of trajectory and thermal maturity in incoming sediments

The diversity in the trajectory of sediments in the wedge leads to a plethora of pathways in which the sediments can become thermally mature and thus introduces epistemic uncertainty in the estimation of maximum exposure temperature. Fig. 6, captures this uncertainty where we plot the maximum exposure temperature as a function of $\%R_o$ for all the models simulated in this study. The colours in for individual markers represent the depth of the markers normalized by the thickness of the wedge represented as Y_n (See Fig S16 for mode details). We find that almost all the models show a remarkable similarity in their relationship between maximum exposure temperature and $\%R_o$ (for individual models please see Fig. S16) and differ mostly in their proportion of sediments with extreme values of $\%R_o$. We observe that the typical uncertainty in maximum exposure temperature increases with an increase in values of $\%R_o$ with ~ 15°C interval at around $\%R_o$=0.2 compared to ~33°C interval at $\%R_o$= 3 (both for 95% confidence interval, Fig. 6b). Moreover, we observe that incorporating information about the normalized depth of sediments (Y_n) significantly aids in constraining the maximum exposure temperature. For instance, although the overall uncertainty at $\%R_o$=1, is ~23°C, for sediments with a Y_n of 0.2-0.4, the uncertainty greatly reduces to only ~10.5°C. Thus, the range of thermal maturity values for sediments clearly has a large correlation with their trajectories.

4.4 Comparison of Easy%R_o, Simple%R_o and Basin%R_o

The usage of Easy%R_o, Simple%R_o, and Basin%R_o in our models provides us with a distinct perspective on the comparative (dis)advantages of each method in estimating thermal maturity values. The non-uniqueness of maximum exposure temperatures for the same values of $\%R_o$ arises from the variation in sediment trajectory and thermal exposure. This diversity among sediment markers results in multiple markers attaining the same level of thermal maturity. We refer to the range of maximum exposure temperatures corresponding to similar $\%R_o$ values as the uncertainty in maximum exposure temperatures. Uncertainty for all three models increases with increasing $\%R_o$ from ~20–25°C at ~0.3 to ~35°C at $\%R_o$=3.5 (Fig. 6b). Easy%R_o, probably the best-recognised method of thermal maturity computation, yields the best constraint on uncertainty for very small changes nearing <1 values. For the values of $\%R_o$ between 1 and 3, all models yield very similar uncertainty, with Simple%R_o yielding the most constrained exposure temperatures (Fig. 6b). However, beyond $\%R_o = 3$, Simple$\%R_o$ becomes unreliable, with uncertainty in exposure temperatures as high as 55°C at $\%R_o = 4$. Easy$\%R_o$ yields an uncertainty range of ~37°C till $\%R_o = 4.4$, and starts to be unreliable above this value. Basin$\%R_o$ remains consistent until a very high value of $\%R_o \sim 6$, and thus provides the best constraint on the widest range of values of thermal maturity (Fig. 6b).

5. Discussion

The thermomechanical models presented in this study provide (a) an explanation for the trend in thermal maturity observed in accretionary wedges, (b) a new venue to explore the uncertainty in the estimation of maximum exposure temperature using vitrinite reflectance, and (c) an estimate of the minimum lateral distance between the trench and the location of a paleo-thermal anomaly on the subduction plate for it to identified after accretion.

5.1 Thermal maturity distribution and importance of thrusting in wedges

Collectively, our results support a general increase of thermal maturity with depth and landward in accretionary wedges. The thermal maturity increase with depth is primarily the result of progressively larger exposures to higher temperatures as depth of burial increases. On the contrary, the landward increase in thermal maturity is caused by the long-term deformation of sediments accumulated at older times and the exhumation of sediments that were underthrusted as they meet the backstop. Our models demonstrate that the rate of landward thermal maturity increase is faster for thicker wedges, both for the case of sediment near the surface and deep inside the wedge (Fig. 4). This can be attributed to a larger proportion of sediments being exposed to higher temperatures over an extended duration within thicker wedges, but validating this result with natural observations remains challenging, given to the very limited availability of thermal maturity data across natural wedges. Accretionary wedges in our models can be simplified as a system where the subducting oceanic plate acts as the primary heat source, while the seafloor acts as a heat sink. The heat generated through other sources such as shear heating, radioactivity, and advection is relatively insignificant compared to the heat originating from the younger oceanic plate. In our simulations, we consider a relatively younger and hotter oceanic plate of approximately 20 Myr, which is consistent with the accretionary wedge in the Nankai region adjacent to the Kumano forearc basin (Zhao et al., 2021). Given that the convergence rate remains constant across all models, the heat received from the oceanic plate should remain relatively similar. However, as the wedge thickness increases, the temperature gradient between the boundaries of the wedge must become gentler, resulting in a larger portion of the wedge experiencing elevated temperatures. Moreover, frequent advection from the subduction channel also results in elevated temperatures in the core of the wedge. Finally, models with thicker wedges typically exhibit higher décollement strength, leading to increased shear heating at the base of the wedge. Observational studies conducted by Yamano et al. (1992) on the thermal structure of the Nankai accretionary prism have further highlighted that the landward increase in prism thickness is the most significant factor contributing to temperature variations within the wedge. Consequently, the sustained higher temperatures within thicker wedges over time would lead to a higher rate of landward thermal maturity.

Our models show two cases where the above-mentioned trend in thermal maturity is relevantly altered, which we nominate "on-fault increase" and "fault-block inversion". For instance, Fig. 3 shows a steep rise in the thermal maturity of sediments at fault sites. Thermal maturity inversions by thrusting, which are commonplace in accretionary contexts, are the primary cause of thermal maturity differentiation among wedges with similar paleo-thermal structures. During fault-block inversions, the positive gradient of thermal maturity with depth is inverted as relatively mature sediments are thrusted over less mature sediments (Underwood et al., 1992). The strong differentiation in the trajectory of sediments led by thrusting has a larger influence over thermal maturity than their burial depth or their in-wedge location. This novel inference has probably remained concealed thus far due to the large number of parameters that condition thrust development, frequency, length, and thermal state and the lack of high-resolution thermal maturity data.

The thermal maturity that incoming sediments reach also varies periodically as a function of thrust frequency. By examining the lateral and vertical position of incoming sediments and their eventual thermal maturity, we can deduce that the overall movement of sediments in the wedge is predominantly layered but not stationary over time. Changes in the depth of the thermal maturity boundary are less frequent and have larger amplitudes with increased décollement strength, and especially, increased sedimentation rates (Fig. 5). The periodicity in the thermal maturity boundary marks the periodic oscillation of the predominant trajectory followed by incoming sediments, i.e. between accretion (low thermal maturity path) and under-thrusting (high-thermal maturity path). As a result, it should also strongly correlate with the periodicity observed in the evolution of forearc topography (Menant et al., 2020) and the frequency of thrust formation in our models. This is expected, given that thrusts are active over longer mean times, and they channel material toward the décollement more efficiently, in wedges with stronger décollement or increased sedimentation. While sediments at internal and higher structural positions of the wedge are translated toward the surface and have a lower thermal maturity, sediments at external and lower structural positions are translated toward the décollement and have a relatively higher maturity. The entire cycle is repeated with the formation of new in-sequence thrust.

This is a relevant observation for it typifies the causality of particular sediment grains following a high or low maturity path, a long-standing unanswered question (Miyakawa et al., 2019). We corroborate this observation by analyzing the terminal thermal maturity of sediments across a frontal thrust active at a younger age. An example in Fig. 7 shows the thermal maturity of sediments at ~7.5 Myr across a thrust active at ~4 Myr. Whereas this occurs for all thrusts in the wedge, the frontal thrust is particularly pronounced in partitioning sediments into the high and low maturity paths. Thermal maturity correlates with sediment depth weakly near faults and more strongly away from them. The distance of sediment from the frontal thrust dictates the trajectory of sediment grains, and as a result, the pressure-temperature conditions to which they are exposed.

Our results show the need to consider all factors influencing fault frequency when inferring the geothermal history of contractional terrains by means of thermal maturity. In this study, we have considered solely how décollement strength and the rate of trench sedimentation vary the frequency, architecture, and overall behavior of thrusts, and the frontal thrust, as the wedge evolves. Fortunately, this predictive exercise should be relatively straightforward, for the impact of these external factors on the fault structure of wedges has been established (Fillon et al., 2012; Mannu et al., 2016, 2017; Mugnier et al., 1997; Simpson, 2010; Storti and Mcclay, 1995), and the effect of each of these factors can be accounted for when assessing the trajectory of sediments and the distribution of thermal maturity in accretionary wedges. It is nevertheless important to note that the frequency of faults in a wedge can be impacted by many other factors, including hinterland sedimentation (Storti and Mcclay, 1995; Simpson, 2010; Fernández-Blanco et al. 2020), erosion (Konstantinovskaia, 2005; Willett, 1992), and seafloor topography (Dominguez et al., 2000).

5.2. Implications

The main implications of this contribution emerge from its predictive power. Our approach can predict to a precise degree the thermal maturity of sediments and the uncertainty associated with the maximum exposure temperature in accretionary contexts with known structuration. A more accurate quantification of the thermal evolution and thermal state of accreted sediments reduces the uncertainties attached to the location of temperature-led transformations of organic material into hydrocarbons in subduction margins and other accretionary contexts. Such increased accuracy in the distribution of thermally mature sediments may also be applied for improved assessments of the evolution in time of any other geothermal process, including seismic slip, magmatic and metamorphic extent, porosity, compaction, and diagenesis of sediments, and the reconstruction of convergent margins in general (Bostick and Pawlewicz, 1984; Mählmann and Le Bayon, 2016; Rabinowitz et al., 2020; Sakaguchi et al., 2011; Totten and Blatt, 1993; Underwood et al., 1992).

Our simulations also imply that the paleo-thermal information stored in the incoming sediments can only be retrieved if sediments are at appropriate locations with respect to emergent thrusts. We illustrate this using two runs of the same model and tracking an artificial thermal anomaly imposed on incoming sediments at two different locations (Fig. 8). This hypothetical thermal anomaly can be conceptualized as any alteration of the thermal maturity profile of incoming sediments, for example, elevated heat flows by an antecedent magmatic intrusion. While the change in %Ro associated with the short-lived thermal anomaly results in abnormally high values of thermal maturity in both sediment packages, it can only be retrieved for the end-model run of sediments located further from the trench (those in the right panel, Fig. 8B). Contrarily, the end-model run of sediments closer to the trench (those in the left panel, Fig. 8A) shows no signs of discontinuity in the thermal maturity distribution of the wedge. This is because we deliberately placed the thermal anomaly at sites that evolve at two structural locations during the model run, i.e., above and below a yet-undeveloped frontal thrust (Fig. 8). The sediment sector affected by the thermal anomaly closer to the trench is overthrusted by the frontal thrust and remains in a footwall location thereafter (Fig. 8a). In contrast, the homologous sedimentary package further away from the trench is accreted by the frontal thrust and remains in a hanging-wall location (Fig. 8b). Thus, the preservation of the record of an antecedent thermal anomaly is only possible in the former case. We further note that, in our simulations, the entire vertical column of sediments records the thermal anomaly, while in nature, the anomaly may affect only sediments at the deeper locations of the sedimentary pile, which are in turn the sediments that most likely to follow a high-maturity path. We thus regard the possibility of retrieving such antecedent geothermal information as minimal.

Finally, among the three methods of %R_o computation, Easy%R_o and Basin%R_o are more consistent and well-constrained on a wide range of thermal maturities in comparison to Simple%R_o, which seems to be particularly useful for a smaller range of thermal maturity values. This simply illustrates the fact that while Easy%R_o and Basin%R_o computation deals with several parallel reactions related to the maturity of kerogen (and hence multiple activation energies), Simple%R_o is based on best-fitted single activation energy, and hence yields large confidence intervals at the extreme %R_o values. Additionally, the inclusion of the higher activation energy reactions in Basin%R_o makes it the best-suited formulation for sediments at the deeper and shear zone sediments which usually get saturated using Easy%R_o.

5.3 Comparisons to previous numerical studies

The thermomechanical models presented in this study offer a dynamic representation of trajectories within the wedge. Although the averaged trends in thermal structure and sediment trajectories remain consistent, there are short-term dynamic fluctuations near the frontal thrust. These fluctuations contribute to a diverse range of sediment paths along the depth of the incoming sediments. Miyakawa et al. (2019) conducted a similar study, modeling vitrinite reflectance using Simple%R_o and a stationary thermal field, which also resulted in an increase in thermal maturity towards the continent and thermal maturity inversions due to thrusting. However, the use of Simple%R_o led to premature saturation and the disappearance of thermal maturity variations at a shallower depth in their model.

We can compare our findings with other geodynamic models that examine the thermal structure of the wedge, although there are only a limited number of numerical models of thermal maturity in wedges. Pajang et al. (2022) recently investigated the distribution of the brittle-ductile transition in wedges and proposed a region dominated by viscous shear near the backstop, with the wedge core reaching temperatures of 450°C and typically containing forearc basins. Although trench sedimentation in our model does not result in the formation of forearc basins, the overall flattening of the wedge slope and the high vitrinite reflectance in the core align with consistent structures. Moreover, the presence of highly mature sediments in the wedge core suggests compacted sediments with greater strength and higher P-wave velocity. Although empirical studies have shown a strong correlation between Vp and thermal maturity estimates for depths of up to 4 km (Baig et al, 2016, Mallick et al. 1995), the exact nature of this correlation may vary depending on the specific location. Nevertheless, the patterns of thermal maturity values in the wedge core in our models also correspond to the patterns of P-wave velocity observed in the Nankai and Hikurangi margins (Górszczyk et al., 2019; Nakanishi et al., 2018; Dewing and Sanei, 2009; Arai et al., 2020).

Two modes of sediment trajectory evolution, from incoming sediment to their position inside the wedge, are generally considered; depth dependence sediment trajectories, as observed in studies by Mulugeta and Koyi, (1992) and Hori and Sakaguchi (2011), and crossover exhumation pathways, as illustrated by Konstantinovskaia et al. (2005) and Miyakawa (2019). We consider the latter as non-stationary sediment trajectories that vary with time and cut across sediment trajectories of sediments previously located at the same spatial position. Our models show that both modes of sediment trajectories are valid, and that changes in trajectory patterns leading to path crossovers are controlled by the horizontal distance of sediments from the frontal thrust. Starting at a threshold distance from the trench, sediments at different depths follow laminar paths along different trajectories within the wedge. Laminar-type trajectories can be reproduced in a broad range of simulations and are particularly common in models with low sedimentation and décollement strengths. However, the depth dependence of sedimentary paths varies periodically as a function of distance from the trench of specific sedimentary packages (Fig. 5). This effect, which is particularly marked in the neighbourhood of the frontal thrust, explains the crossover paths for incoming sedimentary packages at similar depths but different horizontal locations (Konstantinovskaia et al. 2005). Therefore, thrust faults in the wedge act as the primary agent controlling whether sediments sustain depth-controlled laminar flow or sediment mixing.

5.4 Comparisons to natural wedges

Our models achieve thermal maturity distributions that are in good agreement with their natural analogues, despite several relevant assumptions. Our models are very simplified with regard to their natural analogues, with assumptions such as no elasticity, predefined décollement, no erosion, and simple and uniform rheology. Also, our models have an insufficient resolution for small-scale fault activity and lack empirical relations to simulate the compaction of sediments and multiscale fluid flow. Although these assumptions hinder a wholesale comparison between our simulations and natural examples of accretionary wedges, we still find an acceptable agreement between our model and natural observations, primarily due to simulations that have a temperature evolution assimilating empirical data and a fine spatiotemporal resolution. Our estimated %R_o values for the model are in very good agreement with those measured for the borehole C0002 Nankai accretionary wedge by Fukuchi et al. 2009 (Fig. 9). The maximum exposure temperature estimated from the observed thermal maturity for the C0002 borehole also strongly correlates with maximum temperatures recorded on markers in the model with similar thermal maturity with 95% confidence (Fig. S17). However, our result is reliant on the empirical thermal conductivity profiles estimated for the C0002 borehole, which does not show any large thermal discontinuity between the forearc basin and inner wedge that has been observed in fossil accretionary wedges (e.g., Underwood et al. 1989).

Landward increase in thermal maturity is well documented in studies of the Japan trench, at the Miura–Boso plate subduction margin, the fold and thrust belts Western Foothills complex in western Taiwan, the Mesozoic accretionary prism in the Franciscan subduction complex in northern California, as well as Cretaceous Shimanto accretionary complex in Nankai subduction margin (Yamamoto et al. 2017; Sakaguchi et al. 2007; Underwood et al, 1989; Sakaguchi, 1999). The natural wedges mentioned above display vitrinite reflectance values with maximum %R_o values ranging from 0.2 to 4.0 near the surface, which is generally much higher than the near-surface %R_o values observed in our models. Underwood et al. (1989) suggested that this discrepancy is likely due to the ongoing process of progressive exhumation and erosion, leading to the exposure of deeper sections of the accretionary prism over time. As a result, younger wedges, such as those found in the Miura–Boso plate subduction margin, exhibit a much closer resemblance to the %R_o values near the surface of our our models.

On-fault increases in vitrinite reflectance are well also documented in nature, as for boreholes C0004 and C0007, which sample the megasplay fault in Nankai accretionary margin (Sakaguchi et al., 2011). The vitrinite reflectance data from the megasplay and frontal thrusts in Nankai indicate the faults reach a temperature well in excess of 300°C during an earthquake, much larger than the background thermal field. Therefore, on-fault increases in thermal maturity are comparatively smaller in our simulations and lack the marked increase in %Ro observed at fault sites in nature. We consider this is due to a discrepancy in the rate of change of thermal diffusion occurring in simulated thrusts, given that our models develop much wider fault zones than their natural equivalents. For instance, the location of megasplay fault in C0007 borehole exhibits an unevenness within the high-reflectance zone with a maximum %R_o ~1.9 (Sakaguchi et al., 2011). This is in line with the prediction by Fulton and Harris (2012) about the impact of fault thickness on change in vitrinite reflectance. Natural observations also exhibit a much higher incidence of on-fault increase in thermal maturity compared to our simulations, given that our models do not have sufficient spatial resolution to capture the large number of thin faults that develop inside the wedge.

Natural examples of fault-block inversion have been well-documented in natural settings, providing evidence of past thrust activity preserved in the shallower sections of the Nankai accretionary wedge. Sakaguchi (1999) reported the presence of step increments of thermal maturity, similar to increments in vitrinite reflectance in Fig. 3 and 4 across the faults. Other examples are the fault block inversion along the Fukase Fault in the Shimanto accretionary wedge (Ohmori et al., 1997) and the inversion beneath the forearc basin in the Nankai accretionary wedge (Fukuchi et al., 2017).

Our study highlights that paleo-thermal anomalies that extend laterally beyond the average thrust spacing have a significantly higher likelihood of being retained in the final thermal maturity record of the wedge. This allows several inferences. For example, the subduction of the Cretaceous ridge, as identified by Underwood et al. (1993) and Sakaguchi (1999), must have caused a substantial alteration in thermal maturity during the Kula-Pacific subduction in order to be discernible in vitrinite reflectance records. Likewise, we can anticipate the preservation of the paleo-thermal anomaly near Ashizuri in the southern Nankai wedge, which has high thrust frequency, in contrast to that at the Muroto transect, where thrust sheets are widely spaced. In the case of the accretionary wedge adjacent to the Boso peninsula, Kamiya et al. (2017) proposed the emplacement of an ophiolite complex beneath the Miura group. Our findings indicate that the preservation of the thermal-advection heating event coincided with a decrease in trench sedimentation. This likely led to an increase in the thrust frequency, which facilitated the preservation of the thermal-advection heating event in the thermal maturity data.

6. Conclusion

This study demonstrates how contractional faults alter the paths of sediments as they accrete and how this fundamentally controls the distribution of the thermal maturity of sediments in accretionary wedges and emphasizes the role that sedimentation rate and interplate contact strength have in such distribution. The increased resolution of our approach leads to findings that have relevant implications. For example, the geothermal history that can be retrieved from the thermal maturity of sediments in drills, i.e., at the shallow wedge, provides, at best, an incomplete record that is skewed towards the thermal evolution of sediments near the trench. Coevally, relevant sectors of sediments located further seaward, when not subducted, follow high-maturity paths that overprint their antecedent thermal history. Finally, this study also provides a first-order uncertainty measure for the thermal maturity of sediments based on the diversity in their trajectory.

Competing interests

The authors declare that they have no conflict of interest.

References

1. Arai, R., Kodaira, S., Henrys, S., Bangs, N., Obana, K., Fujie, G., ... & NZ3D Team. (2020). Three-dimensional P wave velocity structure of the Northern Hikurangi margin from the NZ3D experiment: Evidence for fault-bound anisotropy. *Journal of Geophysical Research: Solid Earth*, *125*(12), e2020JB020433.
2. Baig, I., Faleide, J. I., Jahren, J., & Mondol, N. H. (2016). Cenozoic exhumation on the southwestern Barents Shelf: Estimates and uncertainties constrained from compaction and thermal maturity analyses. *Marine and Petroleum Geology*, *73*, 105-130.
3. Bostick, N. H., & Pawlewicz, M. J. (1984). Paleotemperatures based on vitrinite reflectance of shales and limestone in igneous dike aureoles in the Upper Cretaceous Pierre shale, Walsenburg, Colorado.
4. Burnham, A. K., & Sweeney, J. J. (1989). A chemical kinetic model of vitrinite maturation and reflectance. *Geo-chimica et Cosmochimica Acta*, *53*(10), 2649-2657.
5. Chi, W. C., & Reed, D. L. (2008). Evolution of shallow, crustal thermal structure from subduction to collision: An example from Taiwan. *Geological Society of America Bulletin*, *120*(5-6), 679-690.
6. Clauser, C., & Huenges, E. (1995). Thermal conductivity of rocks and minerals. *Rock physics and phase relations: a handbook of physical constants*, *3*, 105-126.
7. Davis, D., Suppe, J., & Dahlen, F. A. (1983). Mechanics of fold-and-thrust belts and accretionary wedges. *Journal of Geophysical Research: Solid Earth*, *88*(B2), 1153-1172.
8. DeMets, C., Gordon, R. G., & Argus, D. F. (2010). Geologically current plate motions. *Geophysical journal inter-national*, *181*(1), 1-80.
9. Dewing, K., & Sanei, H. (2009). Analysis of large thermal maturity datasets: Examples from the Canadian Arctic Islands. *International Journal of Coal Geology*, *77*(3-4), 436-448.
10. Dominguez, Stephane, Jacques Malavieille, and Serge E. Lallemand. "Deformation of accretionary wedges in re-sponse to seamount subduction: Insights from sandbox experiments." *Tectonics* 19.1 (2000): 182-196.
11. Fernández-Blanco, D., Mannu, U., Cassola, T., Bertotti G., & Willett SD (2020). Sedimentation and viscosity con-trols on forearc high growth. *Basin Research*, https://doi.org/10.1111/bre.12518

12. Fillon, C., & van der Beek, P. (2012). Post-orogenic evolution of the southern Pyrenees: Constraints from inverse thermo-kinematic modelling of low-temperature thermochronology data. *Basin Research*, *24*(4), 418-436.
13. Fukuchi, M., Nii, T., Ishimaru, N., Minamino, A., Hara, D., Takasaki, I., ... & Tsuda, M. (2009). Valproic acid induces up-or down-regulation of gene expression responsible for the neuronal excitation and inhibition in rat cortical neurons through its epigenetic actions. *Neuroscience research*, *65*(1), 35-43.
14. Fukuchi, R., Yamaguchi, A., Yamamoto, Y., & Ashi, J. (2017). Paleothermal structure of the Nankai inner accretionary wedge estimated from vitrinite reflectance of cuttings. *Geochemistry, Geophysics, Geosystems*, *18*(8), 3185-3196.
15. Gerya, T. V., & Yuen, D. A. (2003). Characteristics-based marker-in-cell method with conservative finite-differences schemes for modeling geological flows with strongly variable transport properties. *Physics of the Earth and Planetary Interiors*, *140*(4), 293-318.
16. Gerya, T. V., & Yuen, D. A. (2003). Rayleigh–Taylor instabilities from hydration and melting propel ‘cold plumes’ at subduction zones. *Earth and Planetary Science Letters*, *212*(1-2), 47-62.
17. Górszczyk, A., Operto, S., Schenini, L., & Yamada, Y. (2019). Crustal-scale depth imaging via joint full-waveform inversion of ocean-bottom seismometer data and pre-stack depth migration of multichannel seismic data: a case study from the eastern Nankai Trough. *Solid Earth*, *10*(3), 765-784.
18. Heki, K., Miyazaki, S. I., Takahashi, H., Kasahara, M., Kimata, F., Miura, S., ... & An, K. D. (1999). The Amurian Plate motion and current plate kinematics in eastern Asia. *Journal of Geophysical Research: Solid Earth*, *104*(B12), 29147-29155.
19. Henrys, S. A., Ellis, S., & Uruski, C. (2003). Conductive heat flow variations from bottom-simulating reflectors on the Hikurangi margin, New Zealand. *Geophysical Research Letters*, *30*(2).
20. Hori, T., & Sakaguchi, H. (2011). Mechanism of décollement formation in subduction zones. *Geophysical Journal International*, *187*(3), 1089-1100.

21. Kamiya, N., Yamamoto, Y., Wang, Q., Kurimoto, Y., Zhang, F., & Takemura, T. (2017). Major variations in vitrinite reflectance and consolidation characteristics within a post-middle Miocene forearc basin, central Japan: A geodynamical implication for basin evolution. *Tectonophysics*, *710*, 69-80.
22. Kimura, G., Hashimoto, Y., Kitamura, Y., Yamaguchi, A., & Koge, H. (2014). Middle Miocene swift migration of the TTT triple junction and rapid crustal growth in southwest Japan: A review. *Tectonics*, *33*(7), 1219-1238.
23. Konstantinovskaia, E., & Malavieille, J. (2005). Erosion and exhumation in accretionary orogens: Experimental and geological approaches. *Geochemistry, Geophysics, Geosystems*, *6*(2).
24. Konstantinovskaya, E., & Malavieille, J. (2011). Thrust wedges with décollement levels and syntectonic erosion: A view from analog models. *Tectonophysics*, *502*(3-4), 336-350.
25. Korup, O., Hayakawa, Y., Codilean, A. T., Matsushi, Y., Saito, H., Oguchi, T., & Matsuzaki, H. (2014). Japan's sediment flux to the Pacific Ocean revisited. *Earth-Science Reviews*, *135*, 1-16.
26. Lin, W., Fulton, P. M., Harris, R. N., Tadai, O., Matsubayashi, O., Tanikawa, W., & Kinoshita, M. (2014). Thermal conductivities, thermal diffusivities, and volumetric heat capacities of core samples obtained from the Japan Trench Fast Drilling Project (JFAST). *Earth, Planets and Space*, *66*(1), 1-11.
27. Maehlmann, R. F., & Le Bayon, R. (2016). Vitrinite and vitrinite like solid bitumen reflectance in thermal maturity studies: Correlations from diagenesis to incipient metamorphism in different geodynamic settings. *International Journal of Coal Geology*, *157*, 52-73.
28. Malavieille, J., & Trullenque, G. (2009). Consequences of continental subduction on forearc basin and accretionary wedge deformation in SE Taiwan: Insights from analogue modeling. *Tectonophysics*, *466*(3-4), 377-394.
29. Mallick, R. K., & Raju, S. V. (1995). Thermal maturity evaluation by sonic log and seismic velocity analysis in parts of Upper Assam Basin, India. *Organic Geochemistry*, *23*(10), 871-879.
30. Mannu, U., Ueda, K., Willett, S. D., Gerya, T. V., & Strasser, M. (2016). Impact of sedimentation on evolution of accretionary wedges: Insights from high-resolution thermomechanical modeling. *Tectonics*, *35*(12), 2828-2846.
31. Mannu, U., Ueda, K., Willett, S. D., Gerya, T. V., & Strasser, M. (2017). Stratigraphic signatures of forearc basin formation mechanisms. *Geochemistry, Geophysics, Geosystems*, *18*(6), 2388-2410.

32. Menant, A., Angiboust, S., Gerya, T., Lacassin, R., Simoes, M., & Grandin, R. (2020). Transient stripping of subducting slabs controls periodic forearc uplift. *Nature communications*, *11*(1), 1823.

33. Miyakawa, A., Kinoshita, M., Hamada, Y., & Otsubo, M. (2019). Thermal maturity structures in an accretionary wedge by a numerical simulation. *Progress in Earth and Planetary Science*, *6*(1), 1-13.

34. Mugnier, J. L., Baby, P., Colletta, B., Vinour, P., Bale, P., & Leturmy, P. (1997). Thrust geometry controlled by erosion and sedimentation: A view from analogue models. *Geology*, *25*(5), 427-430.

35. Mulugeta, G., & Koyi, H. (1992). Episodic accretion and strain partitioning in a model sand wedge. *Tectonophysics*, *202*(2-4), 319-333.

36. Nakanishi, A., Takahashi, N., Yamamoto, Y., Takahashi, T., Citak, S. O., Nakamura, T., ... & Kaneda, Y. (2018). Three-dimensional plate geometry and P-wave velocity models of the subduction zone in SW Japan: Implications for seismogenesis.

37. Nielsen, S. B., Clausen, O. R., & McGregor, E. (2017). basin% Ro: A vitrinite reflectance model derived from basin and laboratory data. *Basin Research*, *29*, 515-536.

38. Ohmori, K., Taira, A., Tokuyama, H., Sakaguchi, A., Okamura, M., & Aihara, A. (1997). Paleothermal structure of the Shimanto accretionary prism, Shikoku, Japan: Role of an out-of-sequence thrust. *Geology*, *25*(4), 327-330.

39. Pajang, S., Khatib, M. M., Heyhat, M., Cubas, N., Bessiere, E., Letouzey, J., ... & Le Pourhiet, L. (2022). The distinct morphologic signature of underplating and seamounts in accretionary prisms, insights from thermomechanical modeling applied to Coastal Iranian Makran. *Tectonophysics*, *845*, 229617.

40. Platt, J. P. (1986). Dynamics of orogenic wedges and the uplift of high-pressure metamorphic rocks. *Geological society of America bulletin*, *97*(9), 1037-1053.

41. Rabinowitz, H. S., Savage, H. M., Polissar, P. J., Rowe, C. D., & Kirkpatrick, J. D. (2020). Earthquake slip surfaces identified by biomarker thermal maturity within the 2011 Tohoku-Oki earthquake fault zone. *Nature communications*, *11*(1), 533.

42. Ruh, J. B. (2020). Numerical modeling of tectonic underplating in accretionary wedge systems. *Geosphere*, *16*(6), 1385-1407.

43. Sakaguchi, A. (1999). Thermal maturity in the Shimanto accretionary prism, southwest Japan, with the thermal change of the subducting slab: fluid inclusion and vitrinite reflectance study. *Earth and Planetary Science Letters*, *173*(1-2), 61-74.

44. Sakaguchi, A., Chester, F., Curewitz, D., Fabbri, O., Goldsby, D., Kimura, G., ... & Yamaguchi, A. (2011). Seismic slip propagation to the updip end of plate boundary subduction interface faults: Vitrinite reflectance geothermometry on Integrated Ocean Drilling Program NanTro SEIZE cores. *Geology*, *39*(4), 395-398.

45. Seno, T., Stein, S., & Gripp, A. E. (1993). A model for the motion of the Philippine Sea plate consistent with NUVEL-1 and geological data. *Journal of Geophysical Research: Solid Earth*, *98*(B10), 17941-17948.

46. Simpson, Guy DH. "Formation of accretionary prisms influenced by sediment subduction and supplied by sediments from adjacent continents." *Geology* 38.2 (2010): 131-134.

47. Storti, F., & McClay, K. (1995). Influence of syntectonic sedimentation on thrust wedges in analogue models. *Geol*

48. Sugihara, T., Kinoshita, M., Araki, E., Kimura, T., Kyo, M., Namba, Y., ... & Thu, M. K. (2014). Re-evaluation of temperature at the updip limit of locked portion of Nankai megasplay inferred from IODP Site C0002 temperature observatory. *Earth, Planets and Space*, *66*(1), 1-14.

49. Suzuki, N., Matsubayashi, H., & Waples, D. W. (1993). A simpler kinetic model of vitrinite reflectance. *AAPG bulletin*, *77*(9), 1502-1508.

50. Sweeney, J. J., & Burnham, A. K. (1990). Evaluation of a simple model of vitrinite reflectance based on chemical kinetics. *AAPG bulletin*, *74*(10), 1559-1570.

51. Tesei, T., Cruciani, F., & Barchi, M. R. (2021). Gravity-driven deepwater fold-and-thrust belts as Critical Coulomb Wedges: Model limitations and the role of friction vs. fluid pressure. *Journal of Structural Geology*, *153*, 104451.

52. Totten, M. W., & Blatt, H. (1993). Alterations in the non-clay-mineral fraction of pelitic rocks across the diagenetic to low-grade metamorphic transition, Ouachita Mountains, Oklahoma and Arkansas. *Journal of Sedimentary Research*, *63*(5), 899-908.

53. Turcotte, D. L., & Schubert, G. (2002). *Geodynamics*. Cambridge university press.

54. Underwood, M. B., Moore, G. F., Taira, A., Klaus, A., Wilson, M. E., Fergusson, C. L., ... & Steurer, J. (2003). Sedimentary and tectonic evolution of a trench-slope basin in the Nankai subduction zone of southwest Japan. *Journal of Sedimentary Research*, *73*(4), 589-602.

55. Underwood, M. B., O'Leary, J. D., & Strong, R. H. (1988). Contrasts in thermal maturity within terranes and across terrane boundaries of the Franciscan Complex, northern California. *The Journal of Geology*, *96*(4), 399-415.

56. Underwood, M. B. (1989). Temporal changes in geothermal gradient, Franciscan subduction complex, northern California. *Journal of Geophysical Research: Solid Earth*, *94*(B3), 3111-3125.

57. Wenk, L., & Huhn, K. (2013). The influence of an embedded viscoelastic–plastic layer on kinematics and mass transport pattern within accretionary wedges. *Tectonophysics*, *608*, 653-666.

58. Willett, S. D. (1992). Dynamic and kinematic growth and change of a Coulomb wedge. In *Thrust tectonics* (pp. 19-31). Dordrecht: Springer Netherlands.

59. Yamano, M., Foucher, J. P., Kinoshita, M., Fisher, A., Hyndman, R. D., Leg, O. D. P., & Party, S. S. (1992). Heat flow and fluid flow regime in the western Nankai accretionary prism. *Earth and Planetary Science Letters*, *109*(3-4), 451-462.

60. Zhao, D., Wang, J., Huang, Z., & Liu, X. (2021). Seismic structure and subduction dynamics of the western Japan arc. *Tectonophysics*, *802*, 228743.

List of Tables

Table 1: Properties for the different materials used for the model runs

Rock Type	Density (kg/m^3)	Cohesion (MPa)	Angle of friction (°)	Thermal Conductivity (W/ (m K))	Flow law	E (kJ/mol)	n
Water	1000	0	0	20		0	0
Air (Sticky-air)	0	0	0	20		0	0
Décollement	2600	0.001	4.5-14.5	(1.5+807/ (T+77))* (1-exp (-Z^2/1.3e7))	Wet quartzite	154	2.3
Sediments1	2600	1/0.05	30/20*	(0.96+807/ (T+77))* (1-exp (-Z^2/1.3e7))	Wet quartzite	154	2.3
Sediments2	2600	1/0.05*	30/20*	(0.96+807/ (T+77))* (1-exp (-Z^2/1.3e7))	Wet quartzite	154	2.3
Upper Continental Crust	2700	1	31	0.64+807/ (T+77)	Wet quartzite	300	2.3
Lower Continental Crust	2800	1	31	0.64+807/ (T+77)	Wet quartzite	300	3.2
Upper Oceanic Crust	3000	1	31	1.18+474/ (T+77)	Plagioclase An75	300	2.3
Lower Oceanic Crust	3000	1	31	1.18+474/ (T+77)	Plagioclase An75	300	3.2
Mantle Lithosphere	3300	1	31	0.73+1293/ (T+77)	Dry olivine	532	3.5
Asthenosphere	3300	1	0.6	0.73+1293/ (T+77)	Dry olivine	532	3.5

**Strain-softened Cohesion/Coefficient of friction*
T is Temperature, Z is the depth from the seafloor.

Table 2: Model runs and their specific characteristic observations

Models	φ_b	φ / φ_{ss}	λ	*SR*	*L*	β(°)	α(°)	α *predicted* (φ_{ss}/φ) (°)	*D*	*<Ro%>*	*%top-half*	*%Bottom-half*
$M_0^{4.5}$	**4.5°**	**30°/20°**	**0**	**None**	**123.2±15.7**	**4.2±0.6**	**0.95±0.3**	**0.03±0.2/-1.3±0.3**	**15.5±7.0**	**0.54**	**0.0**	**12.7**
M_0^{7}	**7°**	**30°/20°**	**0**	**None**	**97.7±9.9**	**4.9±0.8**	**2.6±0.8**	**0.97±0.2/-0.95± 0.3**	**12.1±3.6**	**0.60**	**0.0**	**22.5**
$M_0^{9.5}$	**9.5°**	**30°/20°**	**0**	**None**	**77.8±4.8**	**5.3±0.8**	**3.7±0.9**	**2.1±0.4/-0.32±0.3**	**8.7±2.1**	**0.67**	**0.0**	**31.3**
$M_{0.1}^{9.5}$	**9.5°**	**30°/20°**	**0**	**0.1**	**76.1±5.9**	**5.0±0.9**	**2.3±0.7**	**2.3±0.4/-0.12±0.3**	**7.3±1.1**	**0.71**	**0.1**	**35.3**
$M_{0.3}^{9.5}$	**9.5°**	**30°/20°**	**0**	**0.3**	**79.3±8.2**	**4.9±0.9**	**2.0±0.5**	**2.3±0.4/-0.1±0.3**	**7.8±2.5**	**0.69**	**0.1**	**32.0**
$M_{0.5}^{9.5}$	**9.5°**	**30°/20°**	**0**	**0.5**	**79.9±7.4**	**4.9±0.8**	**2.1±0.5**	**2.3±0.4/-0.1±0.2**	**9.5±4.0**	**0.71**	**2.7**	**34.4**
$M_{0.7}^{9.5}$	**9.5°**	**30°/20°**	**0**	**0.7**	**81.3±10.5**	**5.0±0.9**	**2.1±0.5**	**2.3±0.7/-0.11±0.3**	**9.9±5.0**	**0.73**	**4.2**	**41.5**
$M_{0.9}^{9.5}$	**9.5°**	**30°/20°**	**0**	**0.9**	**82.5±11.0**	**5.0±0.9**	**2.3±0.7**	**2.2±0.4/-0.16±0.3**	**13.8±7.8**	**0.75**	**14.6**	**51.8**
M_0^{12}	**12°**	**30°/20°**	**0**	**None**	**71.6±5.0**	**5.6±1.0**	**5.1±1.0**	**3.5±0.6/0.4±0.4**	**8.8±3.3**	**0.83**	**1.2**	**40.6**
$M_0^{14.5}$	**14.5°**	**30°/20°**	**0**	**None**	**62.7±6.0**	**5.9±1.0**	**6.7±1.4**	**5.1±0.8/1.2±0.4**	**8.0±1.8**	**0.94**	**2.0**	**54.0**

φ_b is décollement Strength (internal angle of friction).
φ Sediment Strength.
φ_{ss} Sediment Strength (Strain weakened)/ (internal angle of friction).
SR Average Sediment rate (mm/yr).
λ is pore-fluid pressure ratio.
L Average Length of the wedge (in km) between ~2.5-7.5Myr. Length of the wedge is computed as the distance between trench and backstop(set at 1850 km from the right edge of the modelling domain).
β Average basal dip angle β (in degrees) between ~2.5-7.5Myr measure by fitting a line in the basal surface.
α Average surface slope angle α (in degrees) between ~2.5-7.5Myr measure computing the slope of fitting the best fitted line in the surface.
D Average Distance between the first and second frontal thrust between ~2.5-7.5Myr (in km). The frontal thrust is always identified from the trench. The send thrust is identified by the high strain rate and deviation of the weak décollement material from the trend of oceanic plate.
α *predicted* (φ_{ss}/φ) is the surface slope predicted using critical wedge theory using the β observed in the model and sediment strength (Initial /Strain weakened).
T Average time a frontal thrust remains active between ~3.5-7.5Myr.
<Ro%> Average vitrinite reflectance of the wedge between ~3.5-7.5 Myr.
%top Proportion of >1 eventual ***Ro% (vitrinite reflectance at 7.5 Myr)*** at shallow half of the incoming sediment at 2.5 Myr.
%bottom Proportion of >1 eventual ***Ro% (vitrinite reflectance at 7.5 Myr)*** at deep half of the incoming sediments.

*Please see Fig. S18 for details on the various measurement done on the wedge.

Table 3: Parameters for Easy%R_o, Simple%R_o and Basin%R_o vitrinite reflectance model.

S. No.	Stoichiometric Coefficient for Easy%R_o (x_{0i_Easy})	Activation Energy for Easy%R_o (kJ/mol) (E_{ai_Easy})	Stoichiometric Coefficient for Simple%R_o (x_{0i_Simple})	Activation Energy(E) for Simple%R_o (E_{ai_Simple})	Stoichiometric Coefficient for Simple%R_o (x_{0i_Basin})	Activation Energy(E) for Basin%R_o (kJ/mol) (E_{ai_Simple})
1	0.0300	142256	1	1.38e5	0.0185	142256
2	0.0300	150624			0.0143	150624
3	0.0400	158992			0.0569	158992
4	0.0400	167360			0.0478	167360
5	0.0500	175728			0.0497	175728
6	0.0500	184096			0.0344	184096
7	0.0600	192464			0.0344	192464
8	0.0400	200832			0.0322	200832
9	0.0400	209200			0.0282	209200
10	0.0700	217568			0.0062	217568
11	0.0600	225936			0.1155	225936
12	0.0600	234304			0.1041	234304
13	0.0600	242672			0.1023	242672
14	0.0500	251040			0.076	251040
15	0.0500	259408			0.0593	259408
16	0.0400	267776			0.0512	267776
17	0.0300	276144			0.0477	276144
18	0.0200	284512			0.0086	284512
19	0.0200	292880			0.0246	292880
20	0.0100	301248			0.0096	301248
$A_{Easy} = 1e13$ and $\%R_{o0} = 0.2$, $A_{Simple} = 1e13$ and $\%R_{o0} = 0.2$, $A_{Basin} = 9.7029e12$ and $\%R_{o0} = 0.2104$						

List of Figures

Fig. 1:

Initial model setup. A. The lithological and geothermal map of the whole computational domain with boundary conditions. B. The zoomed lithological and geothermal map of the inset illustrates the junction of continental and oceanic plates. The colors represent different lithology of the materials used in the models, with upper and lower crust represented by light and dark grey, upper and lower oceanic crust represented by dark and light green. The arrows around the computational domain represent the imposed boundary conditions, while the white contour lines (dashed in the zoomed panel) show the geothermal gradients used for the initial model. The numbers on the white contour lines represent the temperature values in ℃ for the contour.

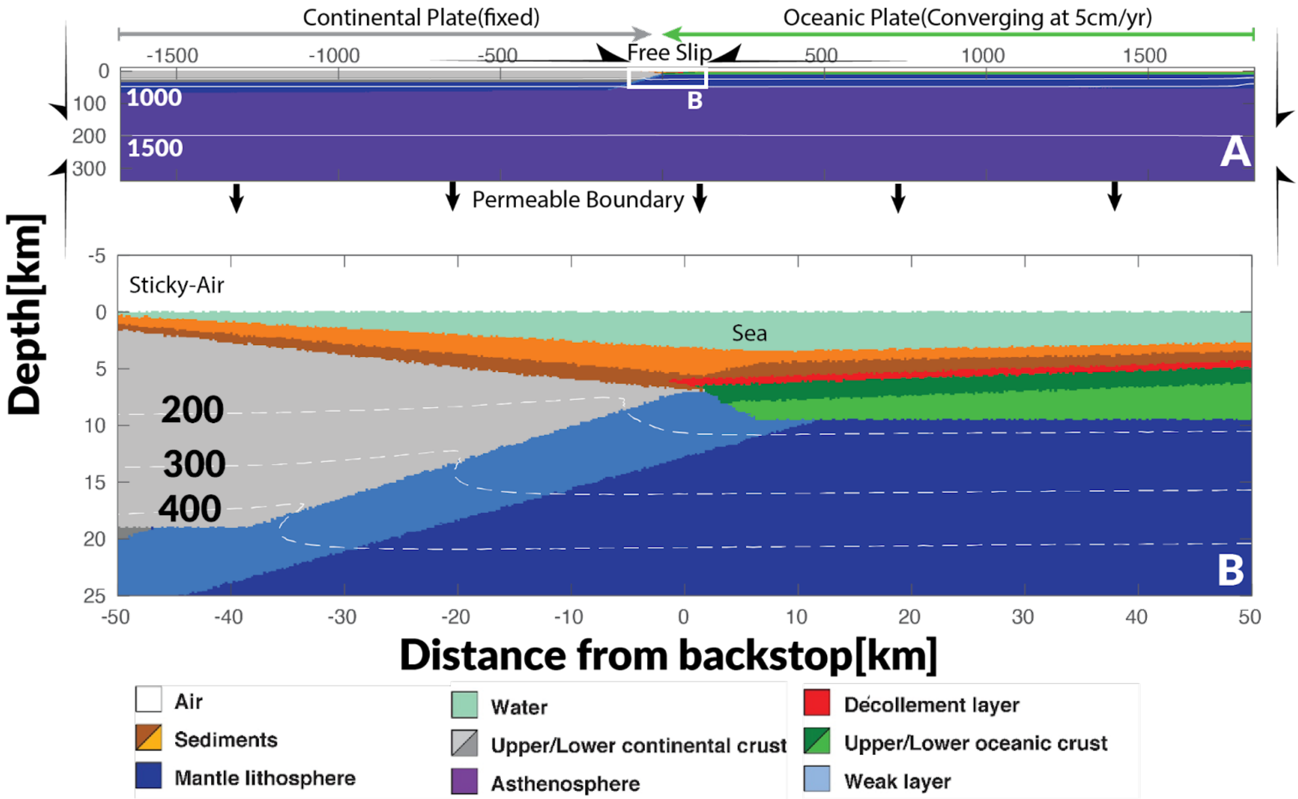

Fig. 2:

Typical thermomechanical evolution of the accretionary wedge for model. The illustrated Figure is for the model $\mathbf{M}_{\mathbf{0}}^{\mathbf{7}}$ *at (a)0.5 Myr (b)2.5 Myr (c)5.0 Myr (d) 7.5 Myr. Similar Figures for other models have been illustrated in supplementary images. The colormap for the panels is same as Figure 1.*

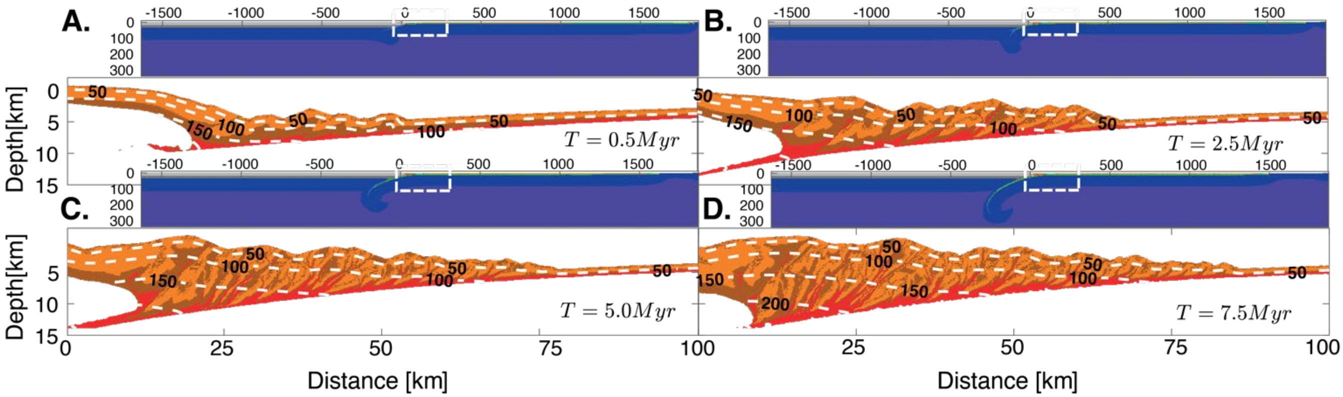

Fig. 3:

Distribution of thermal maturity for different models at ~6.0 Myr (3.5 Myr of thermal maturation). Panels A1-A5 show the thermal maturity distribution (computed using Easy%R_o) in subduction wedges of models as a function of décollement strength , respectively. A6-A10 show the thermal maturity distribution in subduction wedges of models function of sedimentation rae , respectively. The grey color of the markers indicate that no thermal maturity change in these sediments have not occurred. B1-B10 and C1-C10 similarly show the thermal maturity distribution in subduction wedges computed using Simple%R_o and Basin%R_o , respectively.

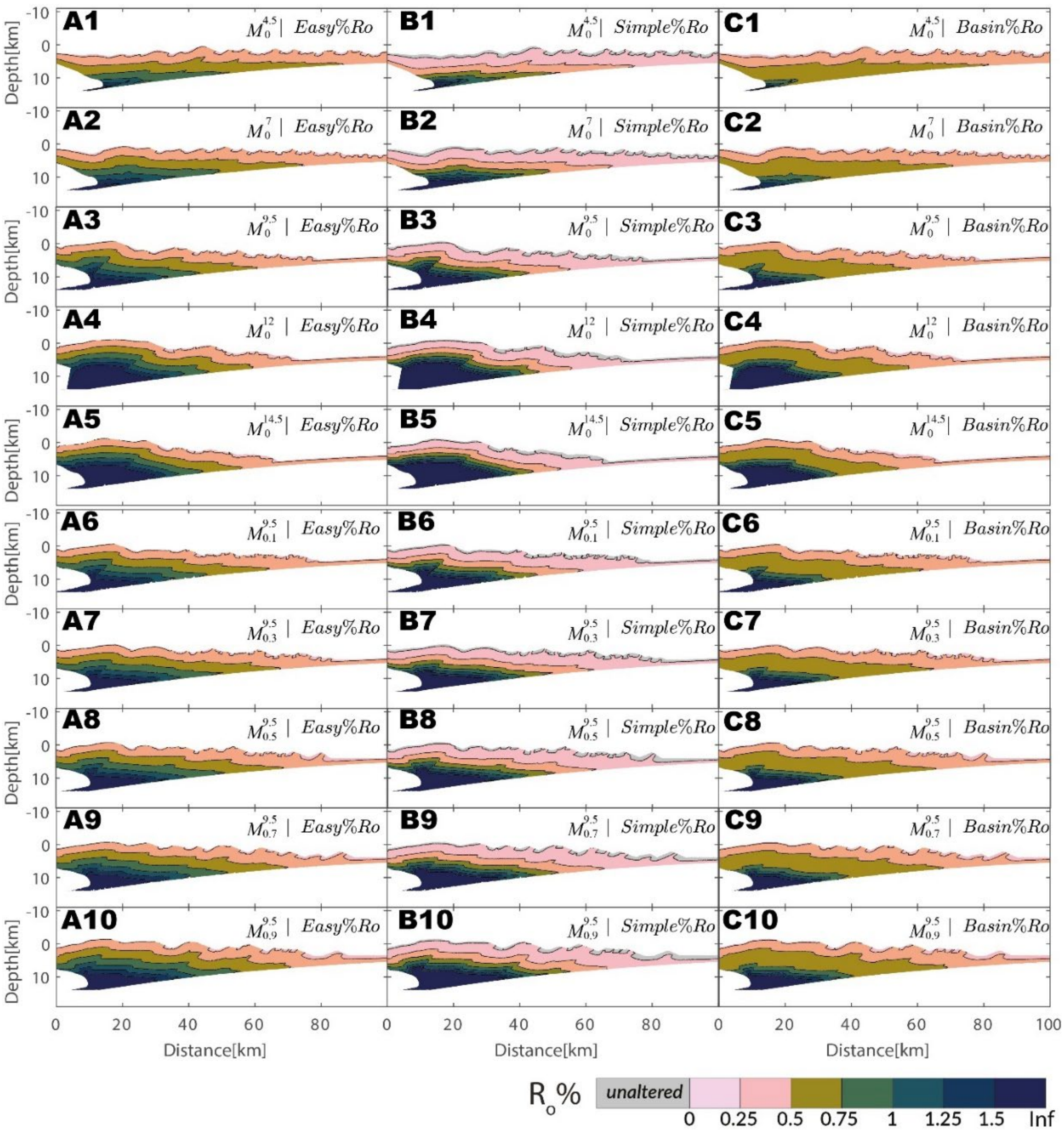

Fig. 4:

The variation of %R_o for a horizon as indicated by the orange band in the inset at 7.5 Myr. Panel A1 and A2 shows all the models with different decollement strength. Panel B1 and B2 shows all the models with different sedimentation rates. Horizons in panel A1 and B1 are located at 1 km depth from the surface, whole in panel A2 and B2 the horizons are horizontal zones located at the trench depth. The horizontal distance from the backstop is normalized by the wedge length. Horizontal distance 0 represents the fixed backstop and 1 represents the trench.

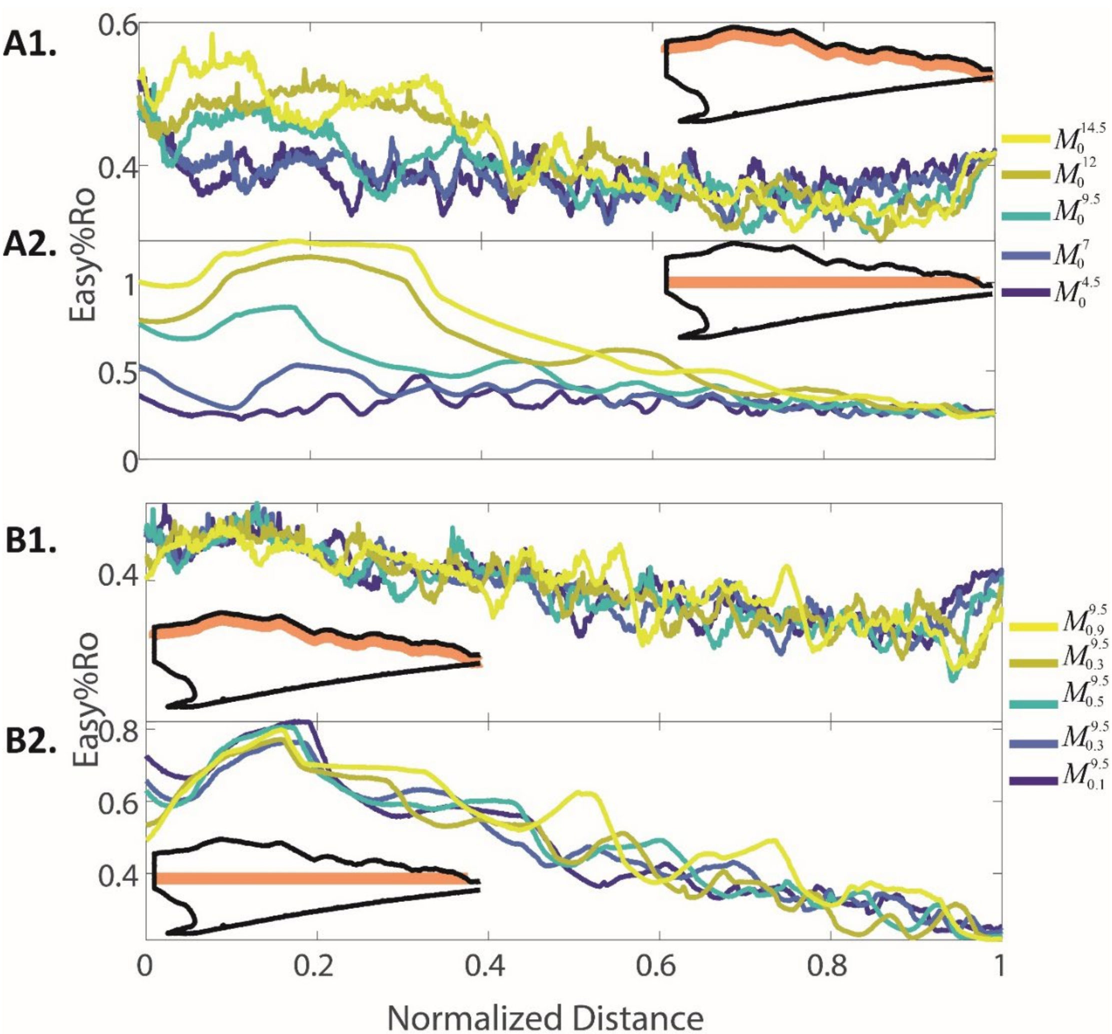

Fig. 5:

Map of thermal maturity at 7.5 Myr mapped to sediments at 2.5 Myr. Panel A1-A5,B1-B5 show the mapping for models - and - respectively. The vertical axis (distance from the oceanic plate) has been corrected for the bending of the plate. The horizontal axis represents the distance of sediments from the trench. The grey colour of the markers indicates that these sediments have been eroded/reworked due to slope failure. The broken black line represents the mean %R_o attained sediment at a given distance from the trench. $\boldsymbol{\Lambda}$ *represents the horizontal periodicity in mean %R_o for the given model.*

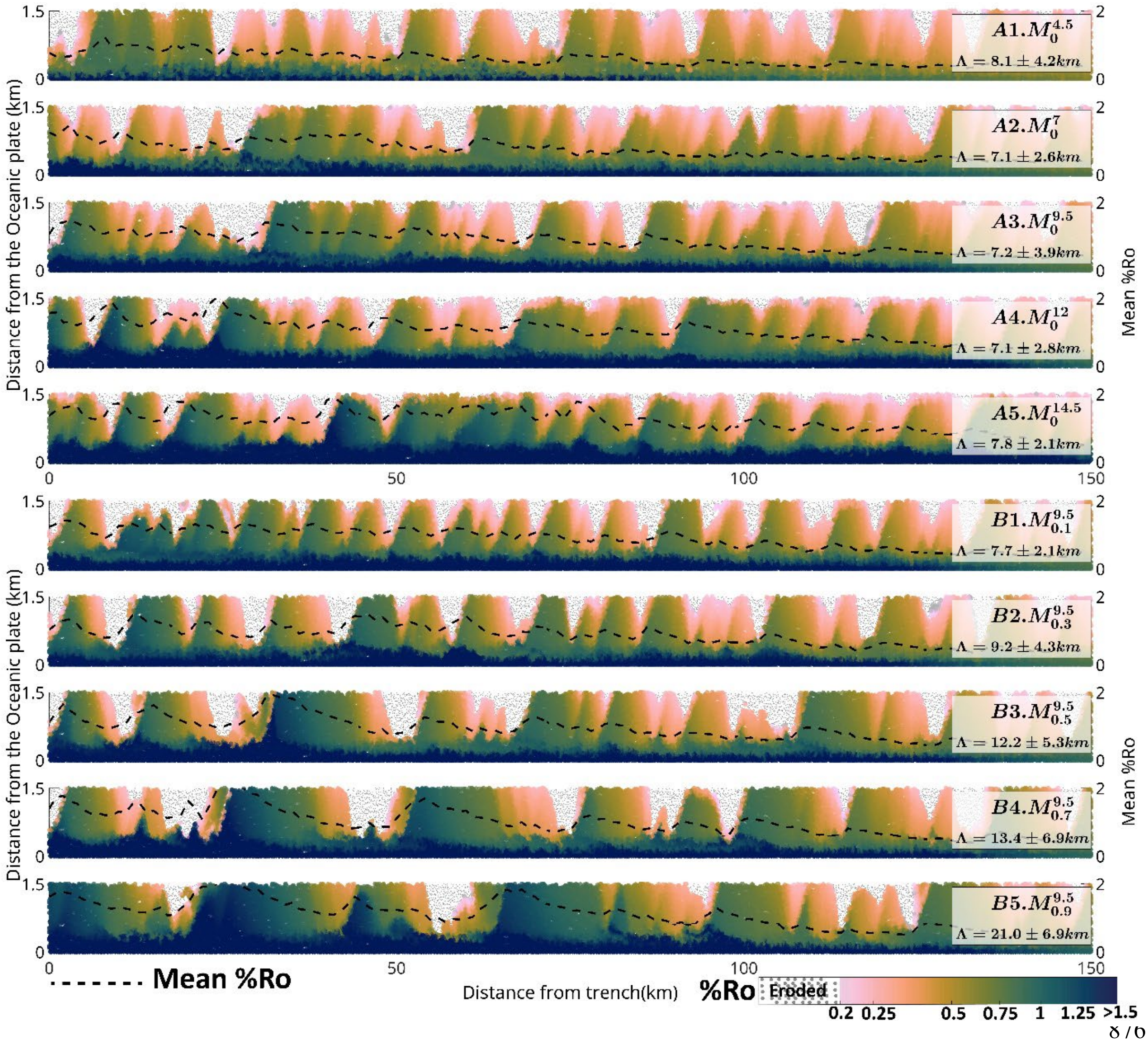

Fig. 6:

A. Vitrinite Reflectance (%R_o) vs Maximum Exposure temperature in all models. The colours in panel A represent the depth of the sediments at 7.5 Myr normalized by the thickness of the wedge (Y_n). B. Range of 95% CI for Easy%Ro, Simple%Ro and Basin%Ro. Y_n is the depth of the marker from the surface normalized by the thickness (vertical extent) of the wedge at the location of the marker. Please see panel B of Fig. S16 for computation of Y_n

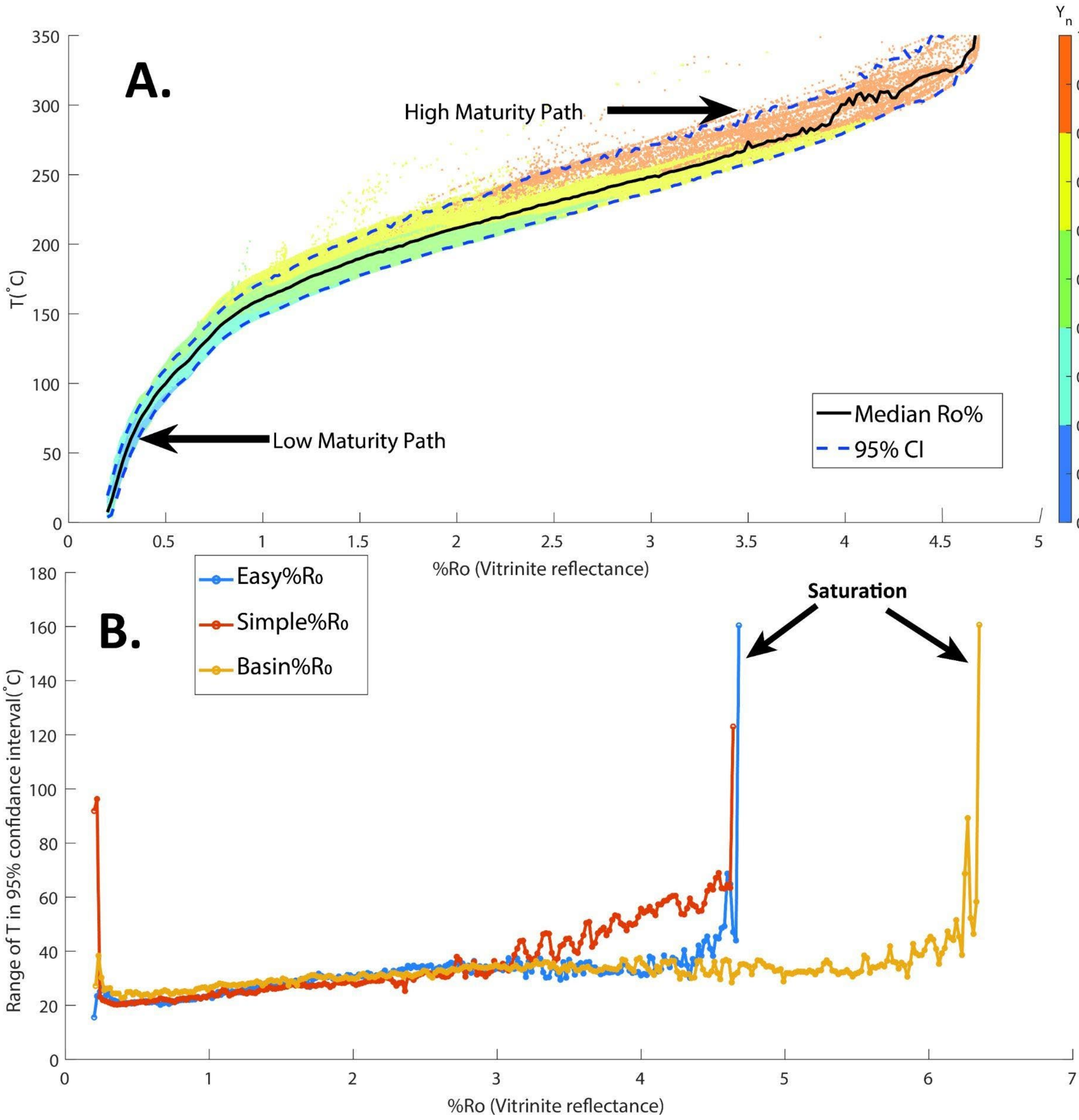

Fig. 7:

Mapping of eventual thermal maturity (vitrinite reflectance at 7.5Myr) to the location of same markers at ~4Myr in model . Panel A shows the values of thermal maturity for the markers while the lithology of the wedge is shown in panel B. The half arrow represents the active frontal thrust. The sediments which were eroded by 7.5Myr but exist at 4Myr have been markers eroded using dotted grey points.

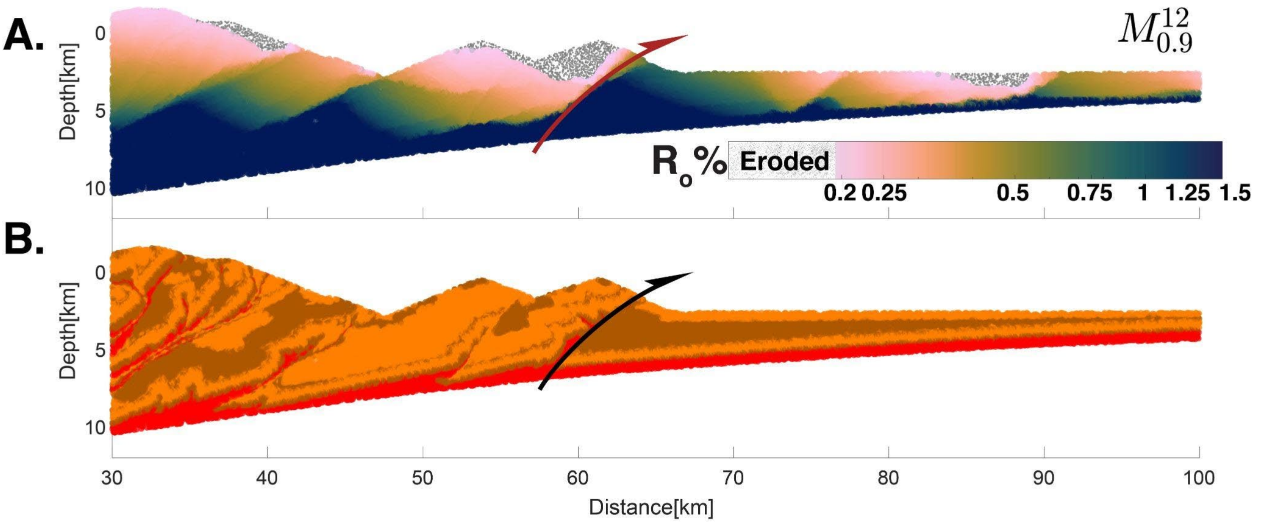

Fig. 8:

Position dependency of thermal maturity preservation. A1. Distribution of %R_o at 2.5 Myr with a paleo-thermal anomaly emplaced at 130-145 km from the backstop. A2. The evolution of the emplaced paleo-thermal anomaly from 2.5 Myr to 6.5 Myr in case 1. A3. Distribution of %R_o at 2.5 Myr. B1. Distribution of %R_o at 2.5 Myr with a paleo-thermal anomaly emplaced at 145-160 km from the backstop. B2. The evolution of the emplaced paleo-thermal anomaly from 2.5 Myr to 6.5 Myr in case 2 B3. Distribution of %R_o at 2.5 Myr with a paleo-thermal anomaly emplaced at 145-160 km from the backstop.

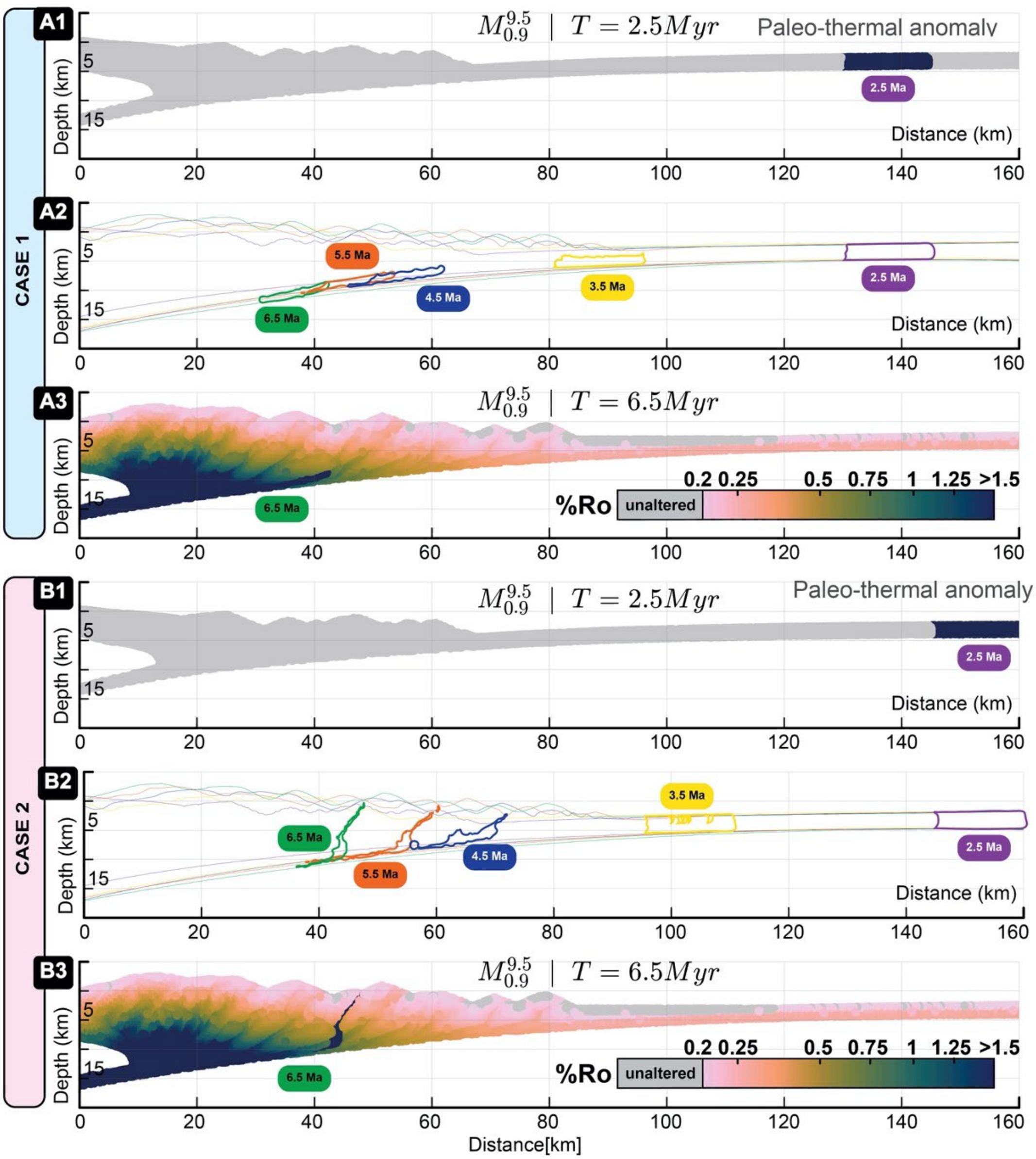

Fig. 9:

Depth vs Thermal maturity (%R_o). The shaded (in voilet) region shows the range of observed R_o% (mean±1SD) from the C0002 borehole ,colored lines represent the values in models sampled from a 10 km wide hypothetical borehole 20km seaward of the backstop as shown in the inset .

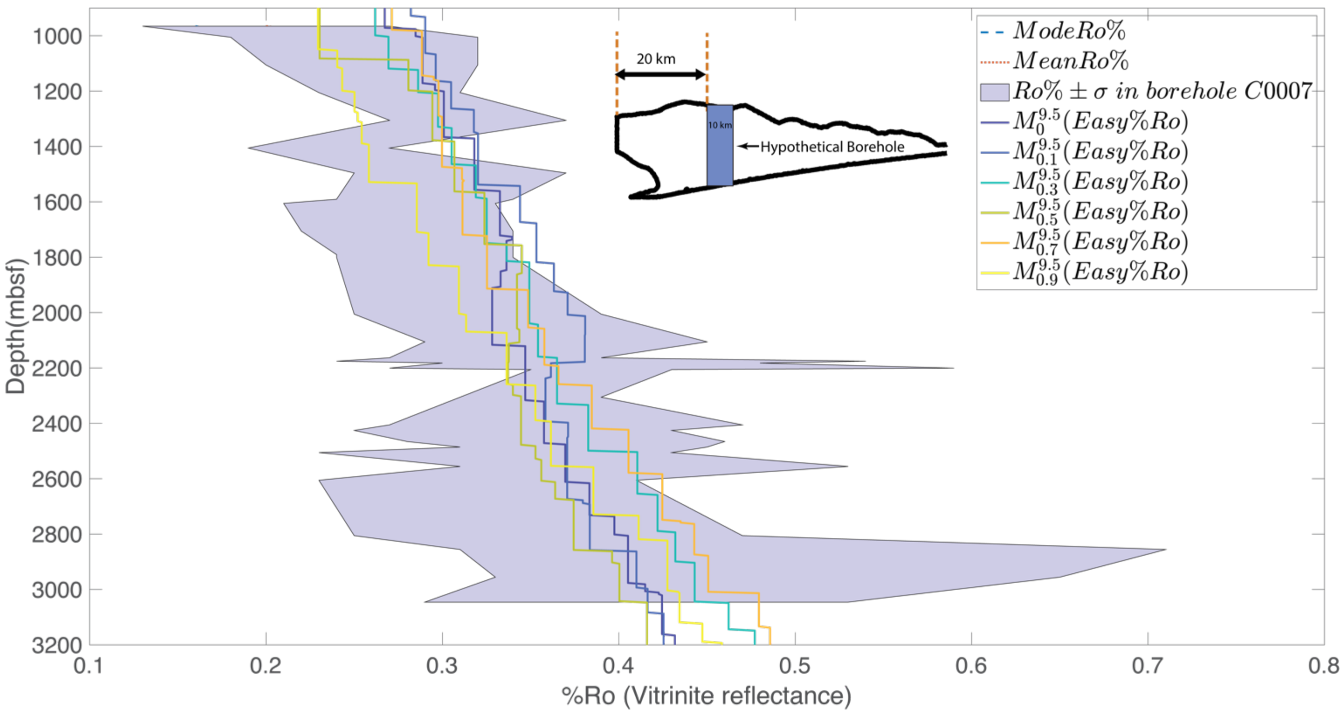

Supplementary Figures

Fig. S1:

Typical Distribution of thermal conductivity in wedge

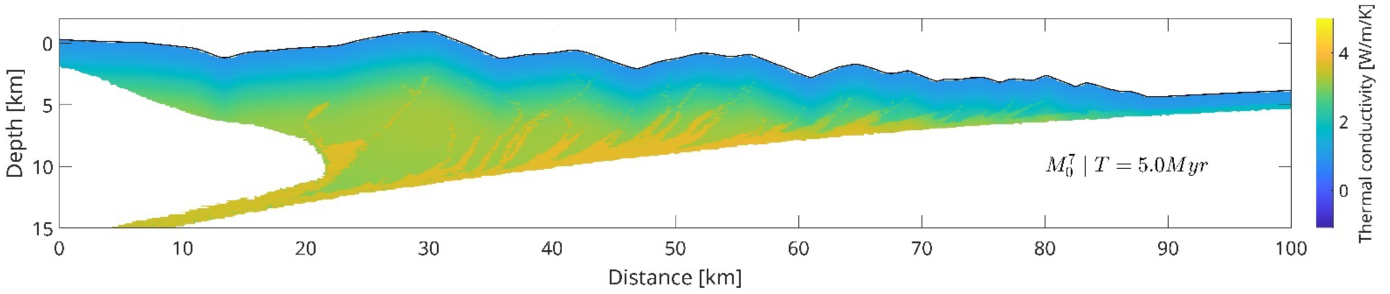

Fig. S2:

Scheme of trench sedimentation in models (taken from (Mannu et al., 2017))

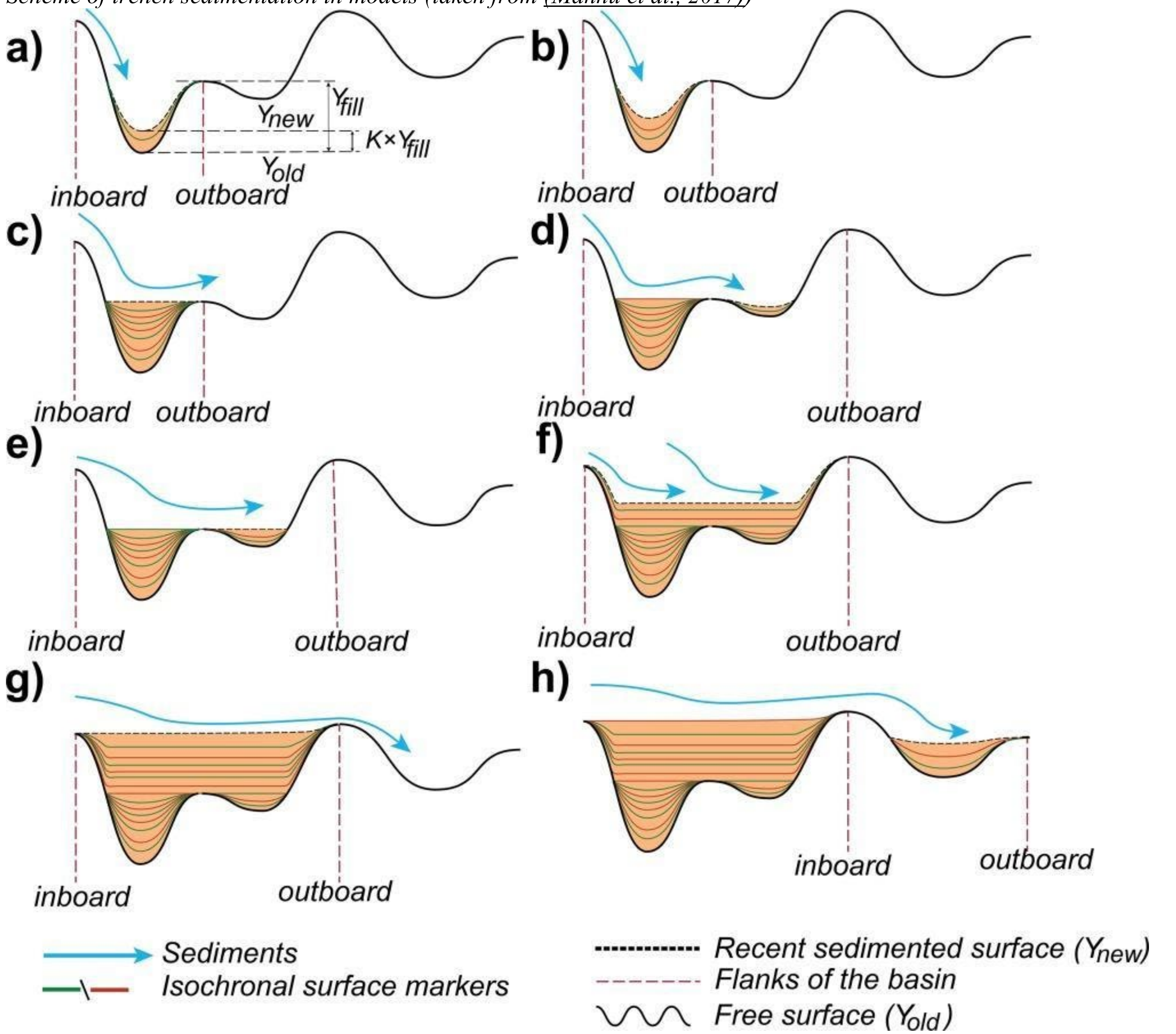

Fig. S3:

Plot of Temperature vs Depth profile in for water-sediment interaction using the data from the International Argo Program and the national programs that contribute for the location(represented by the white square) given in the inset The magenta circle ***represents*** *the Temperature vs Depth profile from the data while the black line is the fitted thermocline used in our models for water-sediment thermal interaction.*

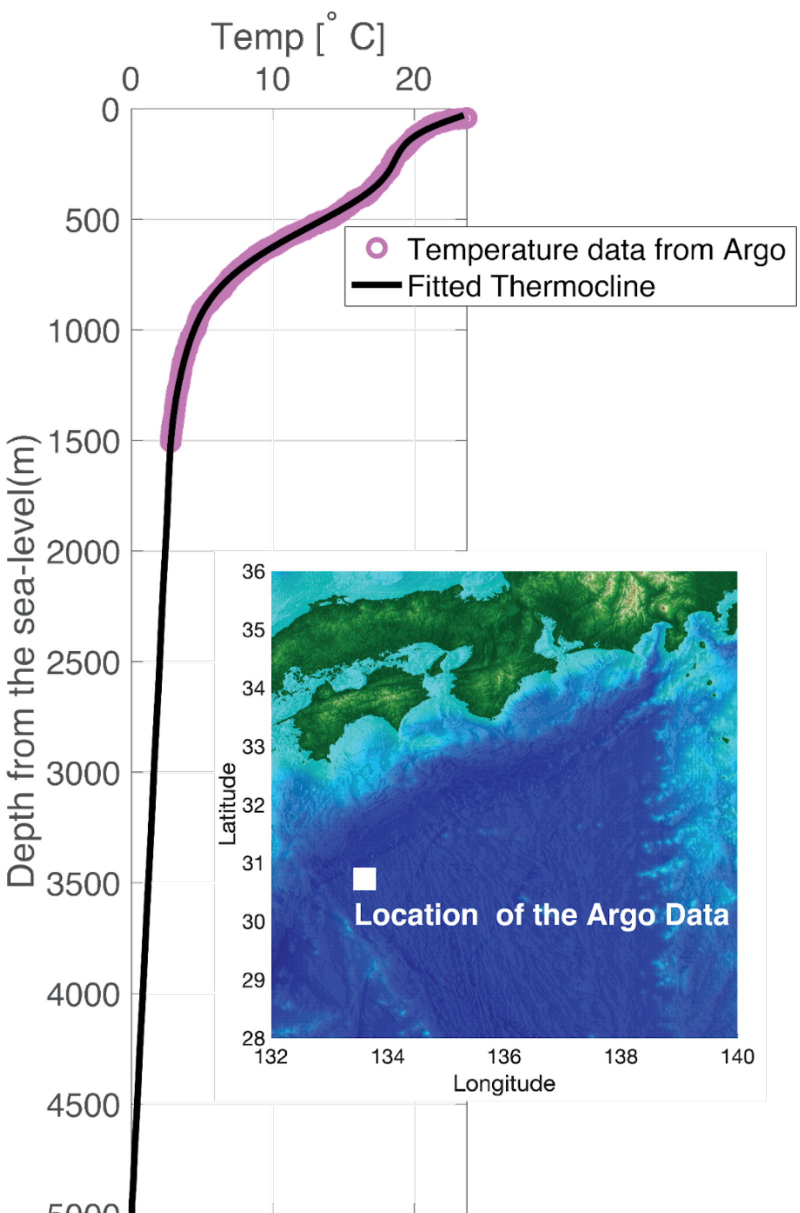

Fig. S4:

Typical thermomechanical evolution of the accretionary wedge for model $\mathbf{M_0^{4.5}}$ *at 0.5 Myr, 2.5 Myr, 5.0 Myr and 7.5 Myr of lithological evolution (Panel A-D). The dashed white lines represent the contours of the temperature field. The colormap for the first 4 panels is same as Figure 1. The last panel represents thermal maturity values at ~7.5 Myr computed using Easy%*R_o*. The colormap for Panel E is same as that of Figure 3.*

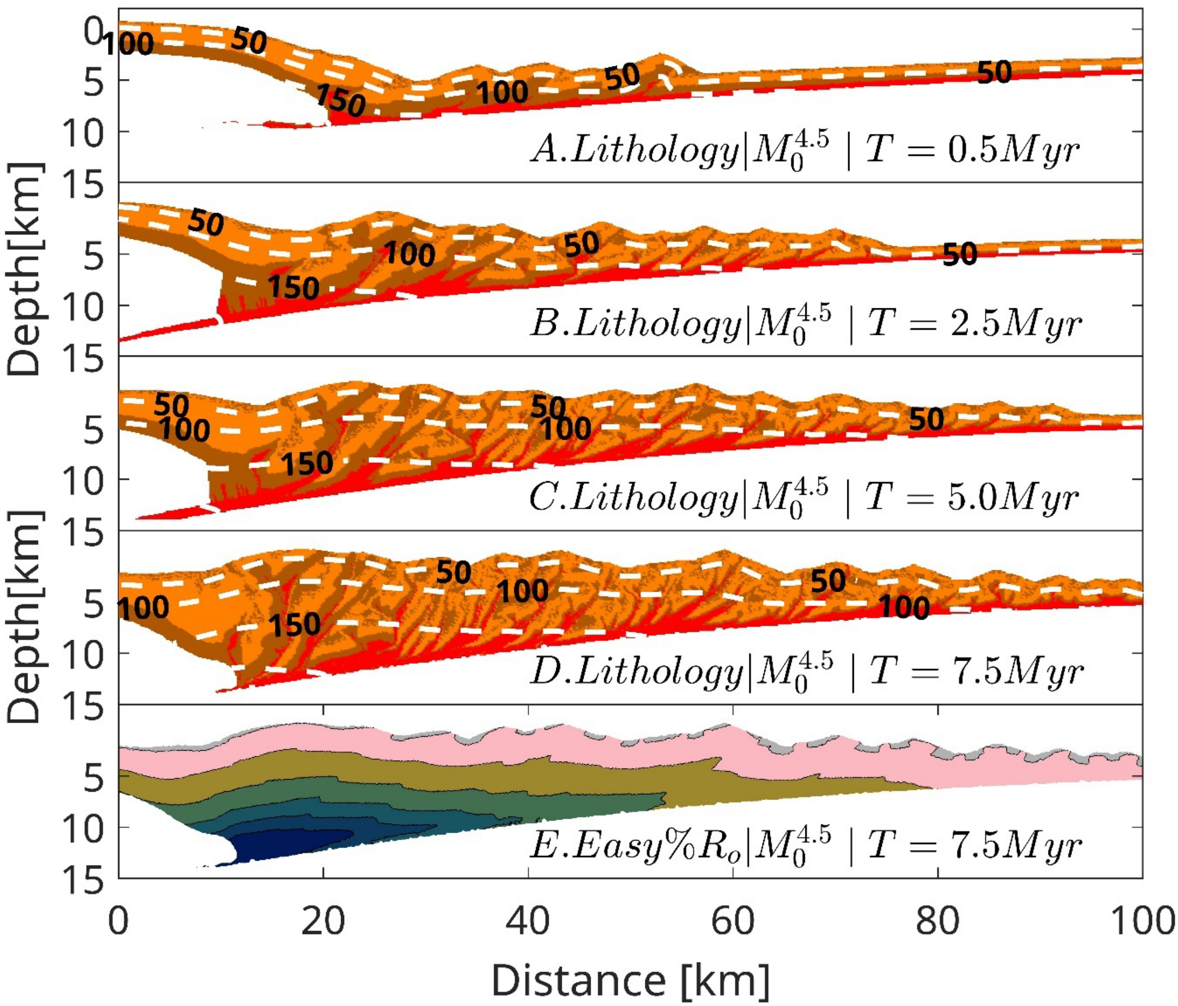

Fig. S5:

Typical thermomechanical evolution of the accretionary wedge for model $\mathbf{M_0^7}$ *at 0.5 Myr, 2.5 Myr, 5.0 Myr and 7.5 Myr of lithological evolution (Panel A-D). The dashed white lines represent the contours of the temperature field. The colormap for the first 4 panels is same as Figure 1. The last panel represents thermal maturity values at ~7.5 Myr computed using Easy%*R_o*. The colormap for Panel E is same as that of Figure 3.*

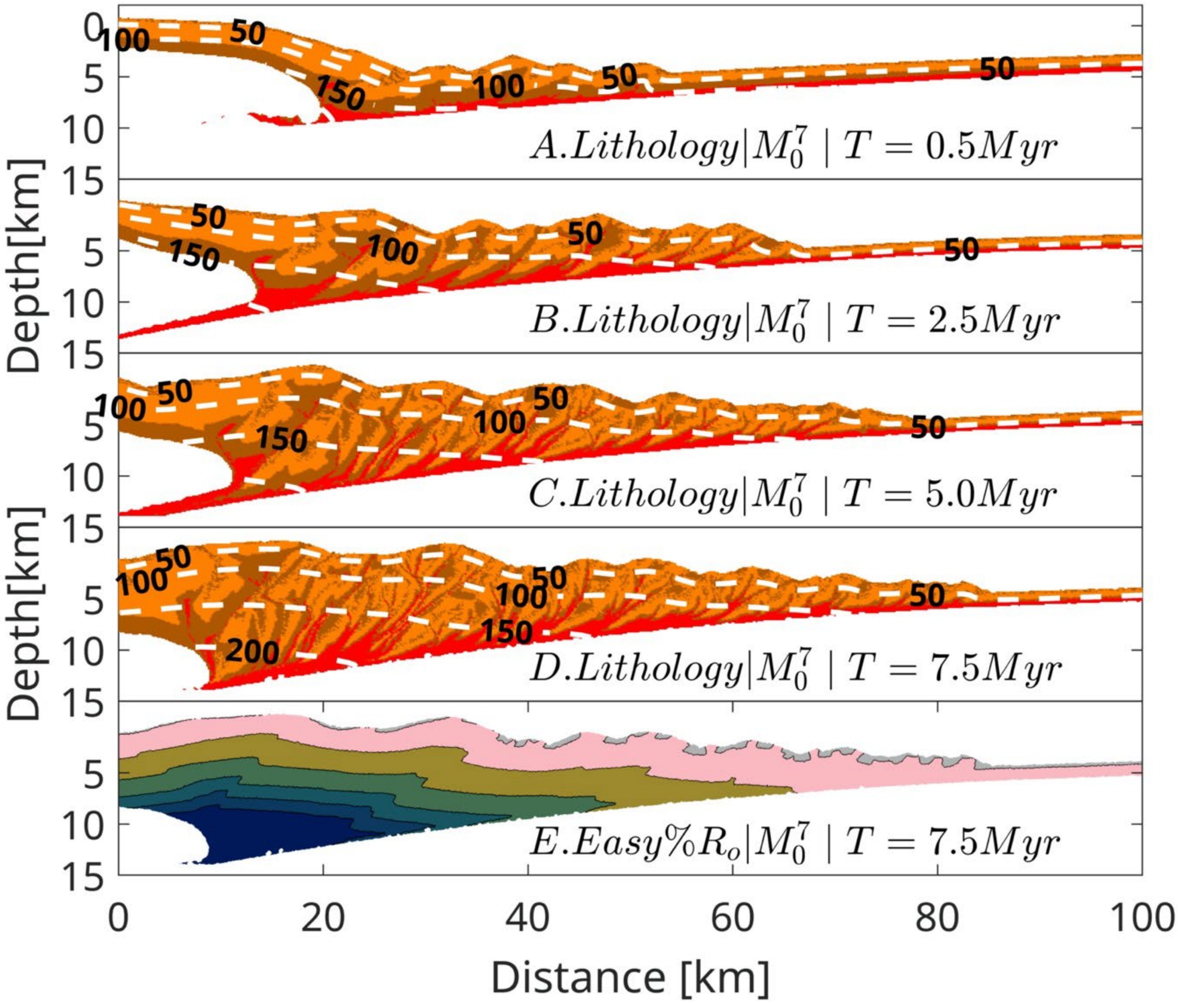

Fig. S6:

Typical thermomechanical evolution of the accretionary wedge for model $\mathbf{M_0^{9.5}}$ *at 0.5 Myr, 2.5 Myr, 5.0 Myr and 7.5 Myr of lithological evolution (Panel A-D). The dashed white lines represent the contours of the temperature field. The colormap for the first 4 panels is same as Figure 1. The last panel represents thermal maturity values at ~7.5 Myr computed using Easy%*R_o*. The colormap for Panel E is same as that of Figure 3.*

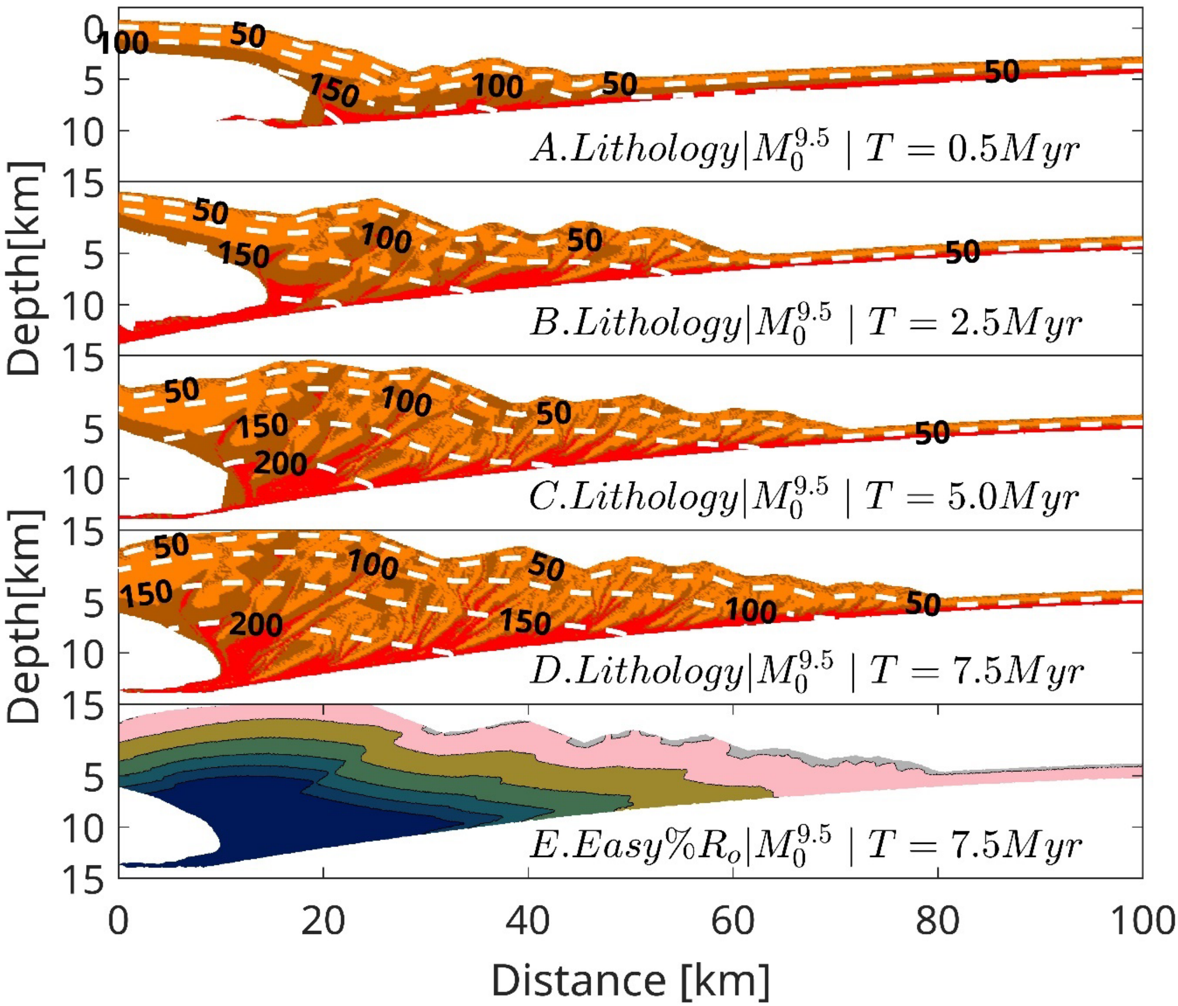

Fig. S7:

Typical thermomechanical evolution of the accretionary wedge for model $\mathbf{M_0^{12}}$ *at 0.5 Myr, 2.5 Myr, 5.0 Myr and 7.5 Myr of lithological evolution (Panel A-D). The dashed white lines represent the contours of the temperature field. The colormap for the first 4 panels is same as Figure 1. The last panel represents thermal maturity values at ~7.5 Myr computed using Easy%Rₒ. The colormap for Panel E is same as that of Figure 3.*

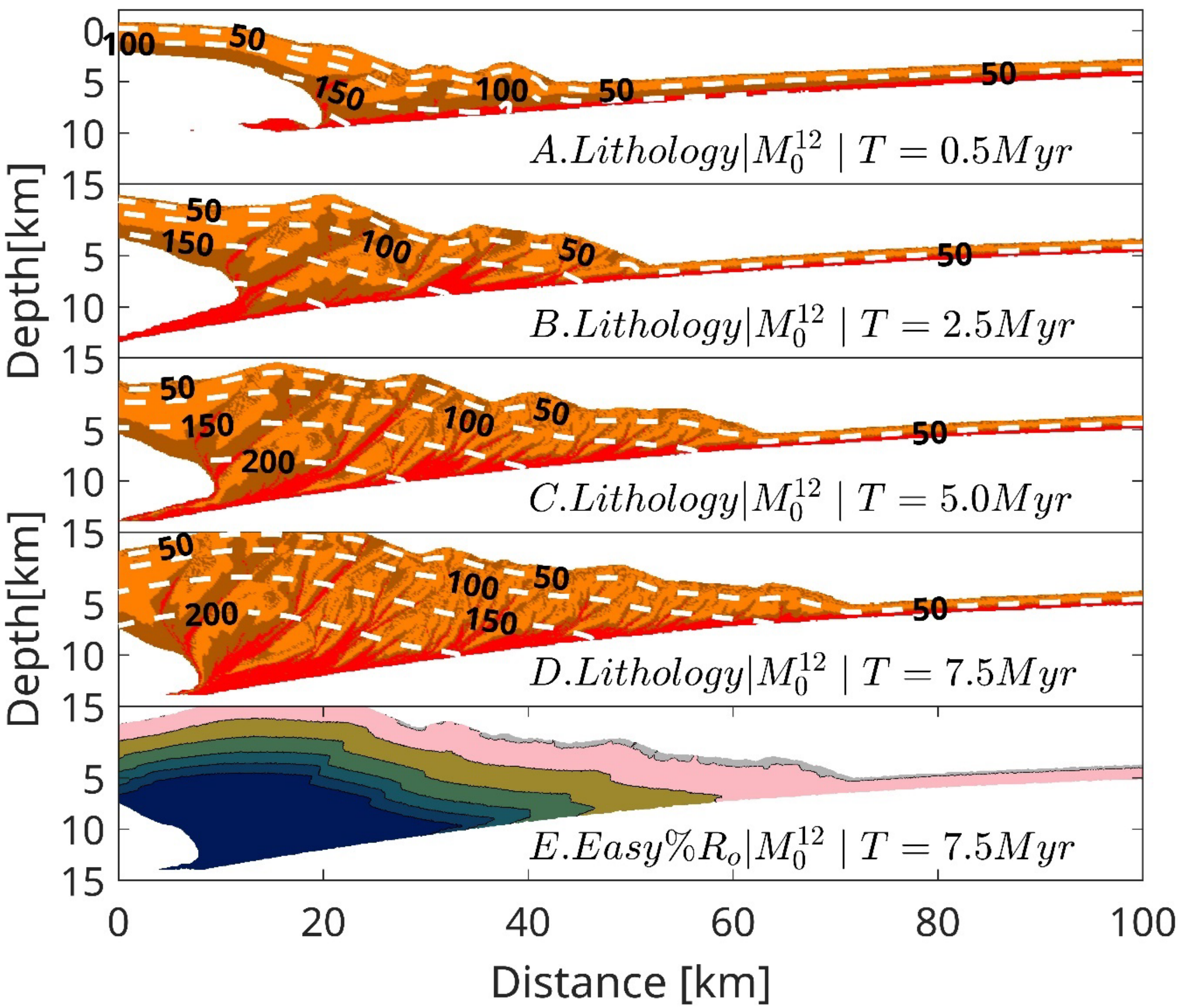

Fig. S8:

Typical thermomechanical evolution of the accretionary wedge for model $\mathbf{M_0^{14.5}}$ *at 0.5 Myr, 2.5 Myr, 5.0 Myr and 7.5 Myr of lithological evolution (Panel A-D). The dashed white lines represent the contours of the temperature field. The colormap for the first 4 panels is same as Figure 1. The last panel represents thermal maturity values at ~7.5 Myr computed using Easy%R_o. The colormap for Panel E is same as that of Figure 3.*

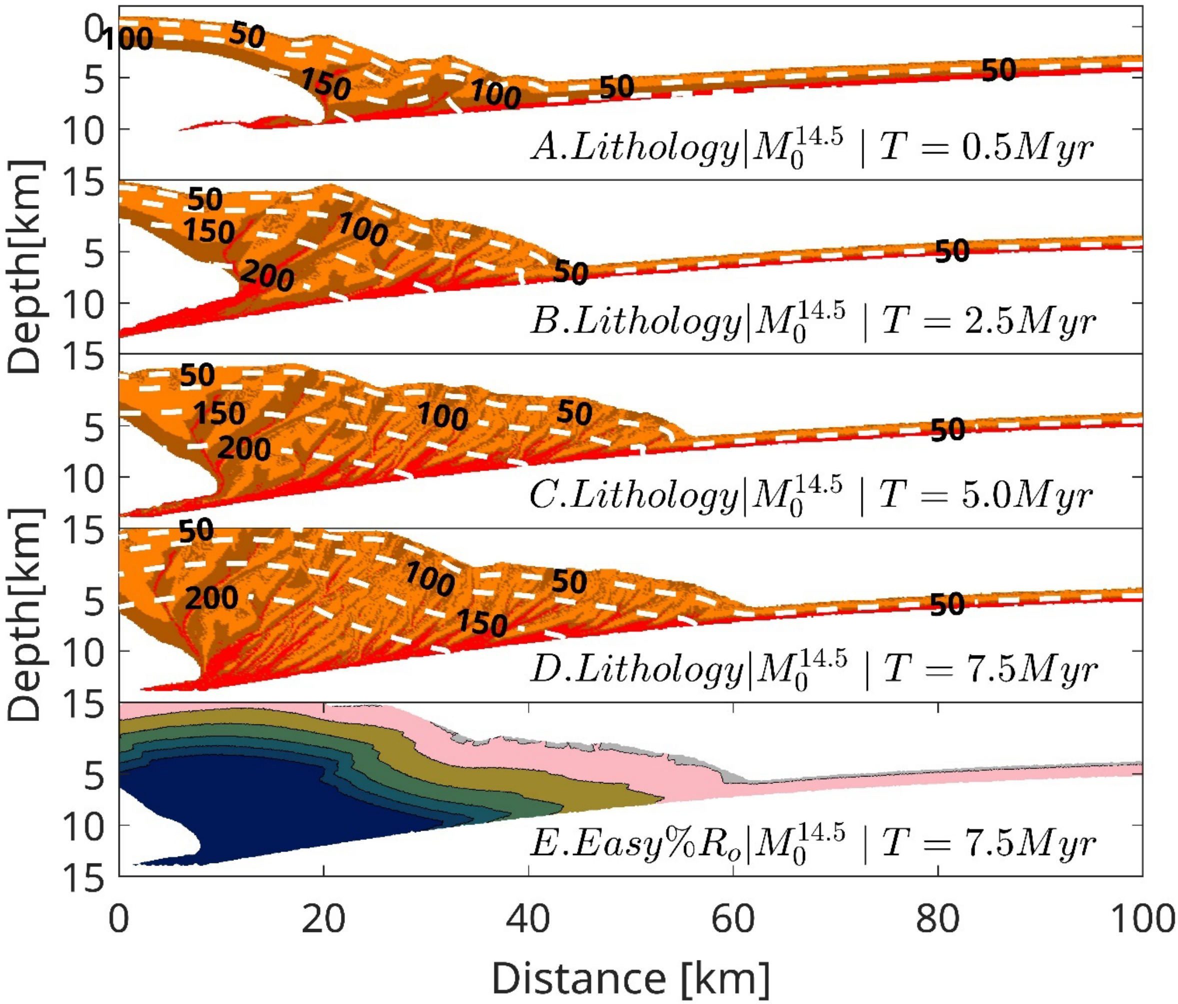

Fig. S9:

Typical thermomechanical evolution of the accretionary wedge for model $\mathbf{M_{0.1}^{9.5}}$ *at 5.0 Myr and 7.5 Myr of lithological evolution (Panel A-B). The dashed white lines represent the contours of the temperature field. The colormap for the first 2 panels is same as Figure 1. The Panel C represents thermal maturity values at ~7.5 Myr computed using Easy%R_o. The colormap for Panel E is same as that of Figure 3.*

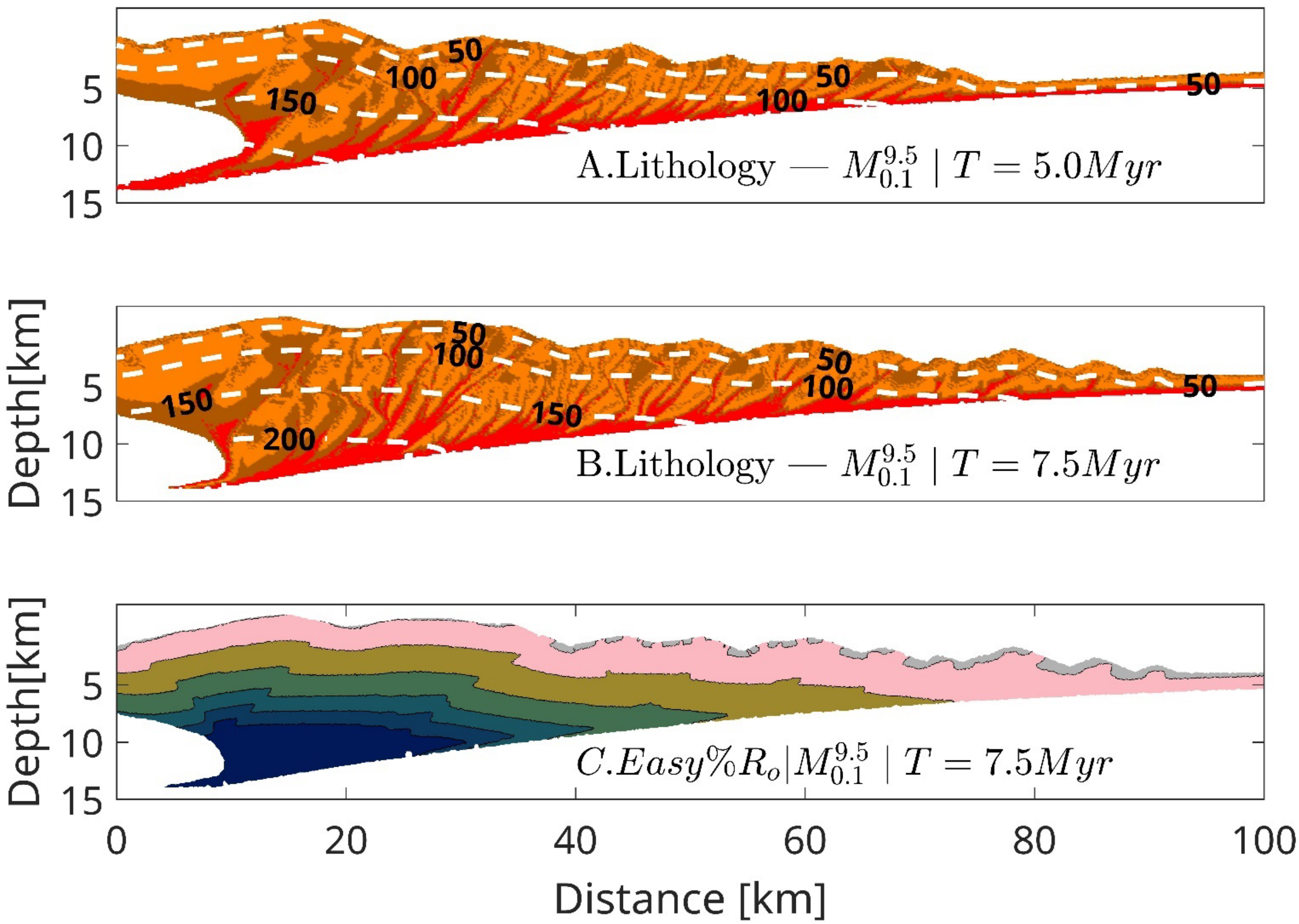

Fig. S10:

Typical thermomechanical evolution of the accretionary wedge for model $\boldsymbol{M_{0.3}^{9.5}}$ *at 5.0 Myr and 7.5 Myr of lithological evolution (Panel A-B). The dashed white lines represent the contours of the temperature field. The colormap for the first 2 panels is same as Figure 1. The Panel C represents thermal maturity values at ~7.5 Myr computed using Easy%*R_o*. The colormap for Panel E is same as that of Figure 3.*

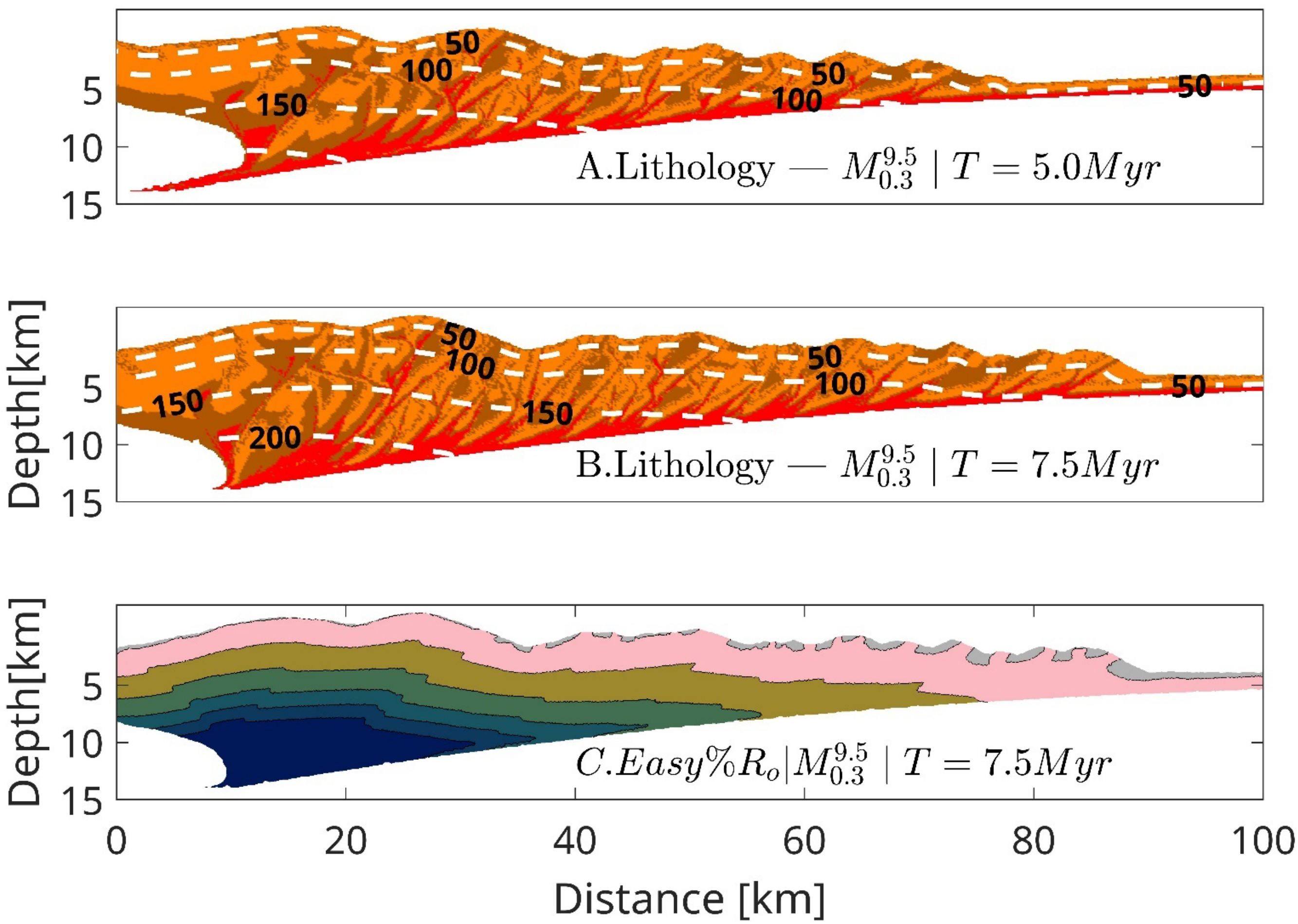

Fig. S11:

Typical thermomechanical evolution of the accretionary wedge for model $\mathbf{M^{4.5}_{0.5}}$ *at 5.0 Myr and 7.5 Myr of lithological evolution (Panel A-B). The dashed white lines represent the contours of the temperature field. The colormap for the first 2 panels is same as Figure 1. The Panel C represents thermal maturity values at ~7.5 Myr computed using Easy%*R_o*. The colormap for Panel E is same as that of Figure 3.*

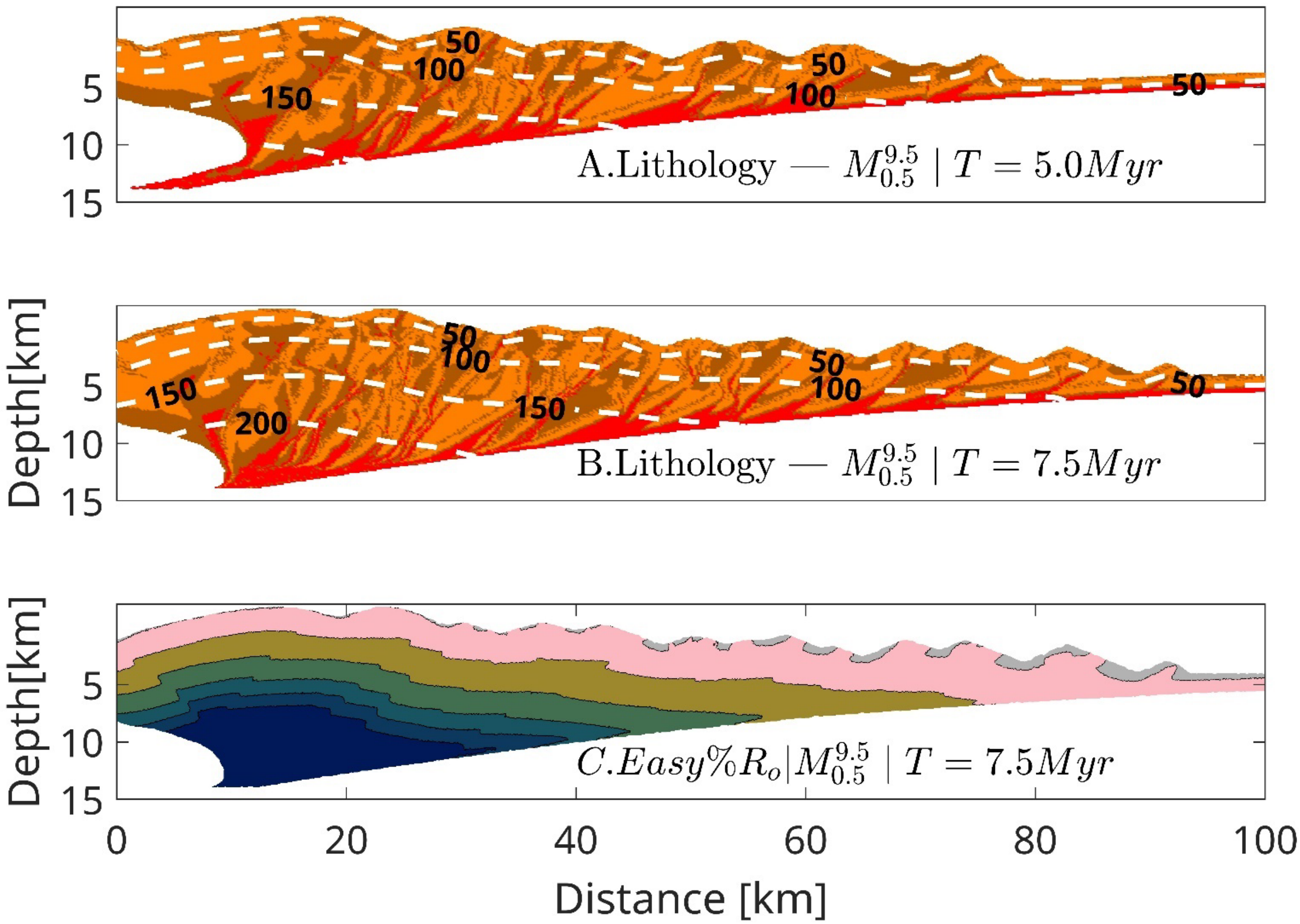

Fig. S12:

Typical thermomechanical evolution of the accretionary wedge for model $\mathbf{M_{0.7}^{9.5}}$ *at 5.0 Myr and 7.5 Myr of lithological evolution (Panel A-B). The dashed white lines represent the contours of the temperature field. The colormap for the first 2 panels is same as Figure 1. The Panel C represents thermal maturity values at ~7.5 Myr computed using Easy%R*$_o$*. The colormap for Panel E is same as that of Figure 3.*

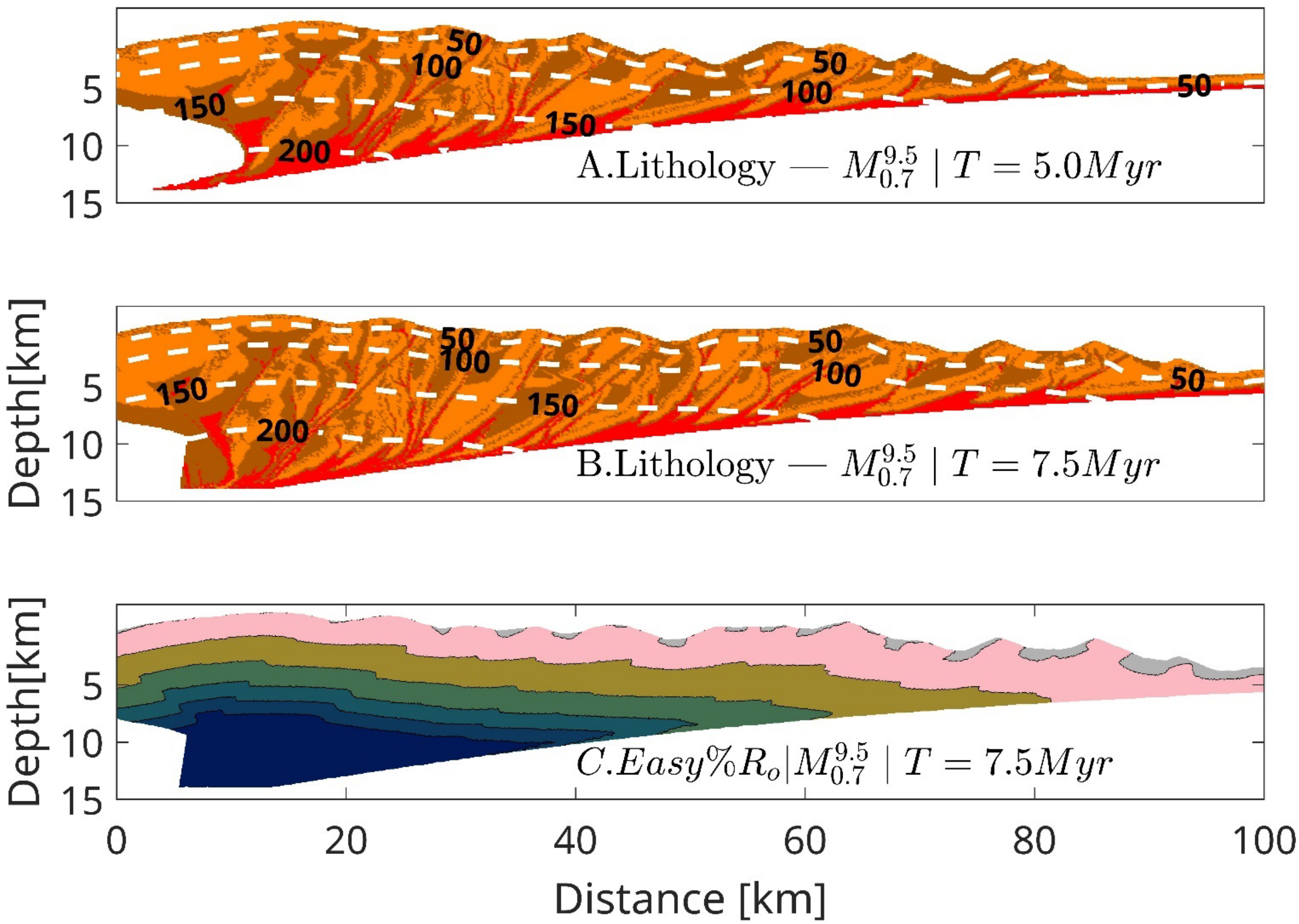

Fig. S13:

Typical thermomechanical evolution of the accretionary wedge for model $\mathbf{M_{0.9}^{9.5}}$ *at 5.0 Myr and 7.5 Myr of lithological evolution (Panel A-B). The dashed white lines represent the contours of the temperature field. The colormap for the first 2 panels is same as Figure 1. The Panel C represents thermal maturity values at ~7.5 Myr computed using Easy%*R_o*. The colormap for Panel E is same as that of Figure 3.*

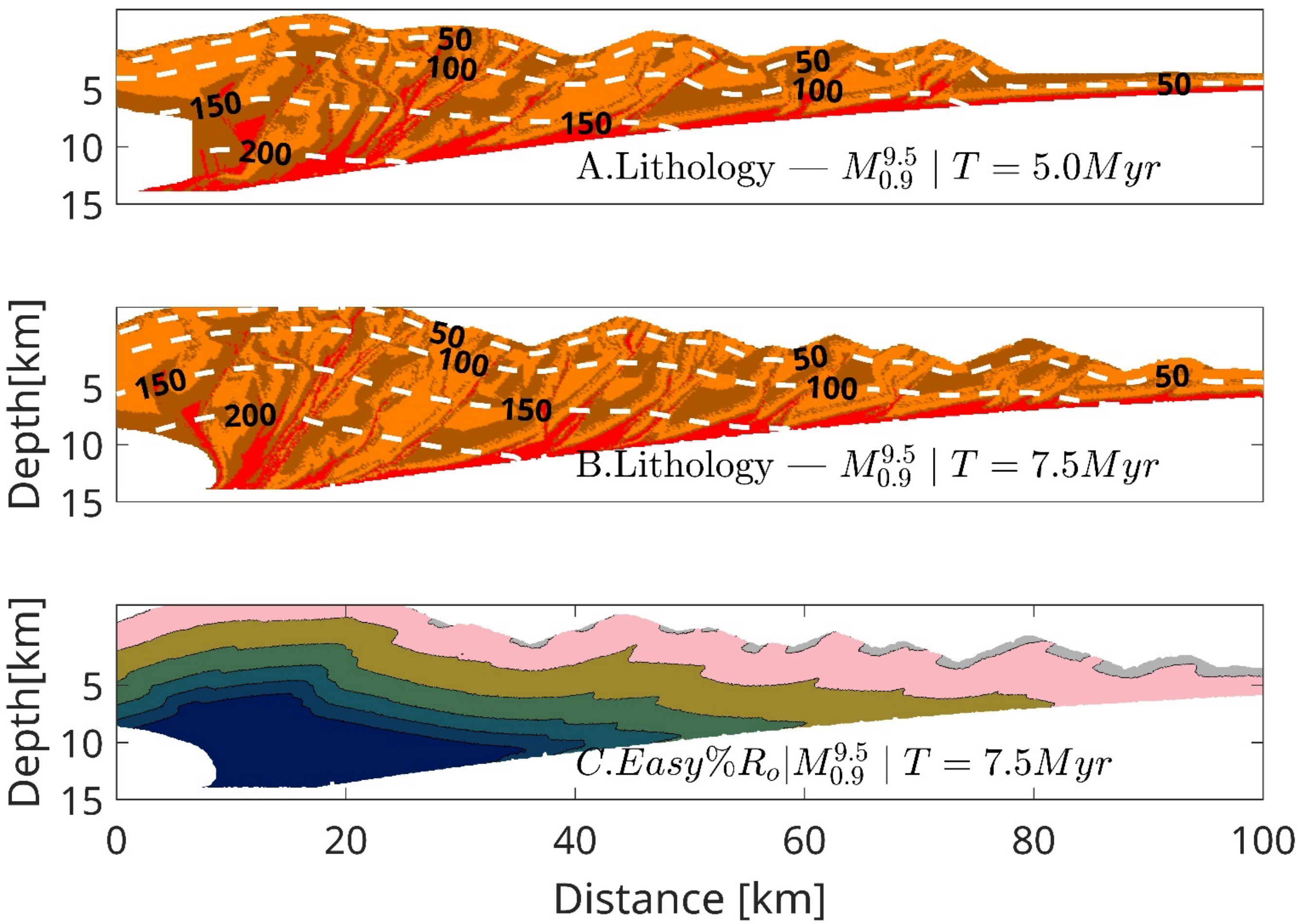

Fig. S14:

Plot of Temperature vs Depth profile in all models compared to Temperature-depth profile based on in-situ temperature from the long-term borehole monitoring system (indicated red patch is the range of temperature estimated by (Sugihara et al., 2014)). The temperature vs depth profiles for the models are computed for 20 kms from the backstop as shown in the inset.

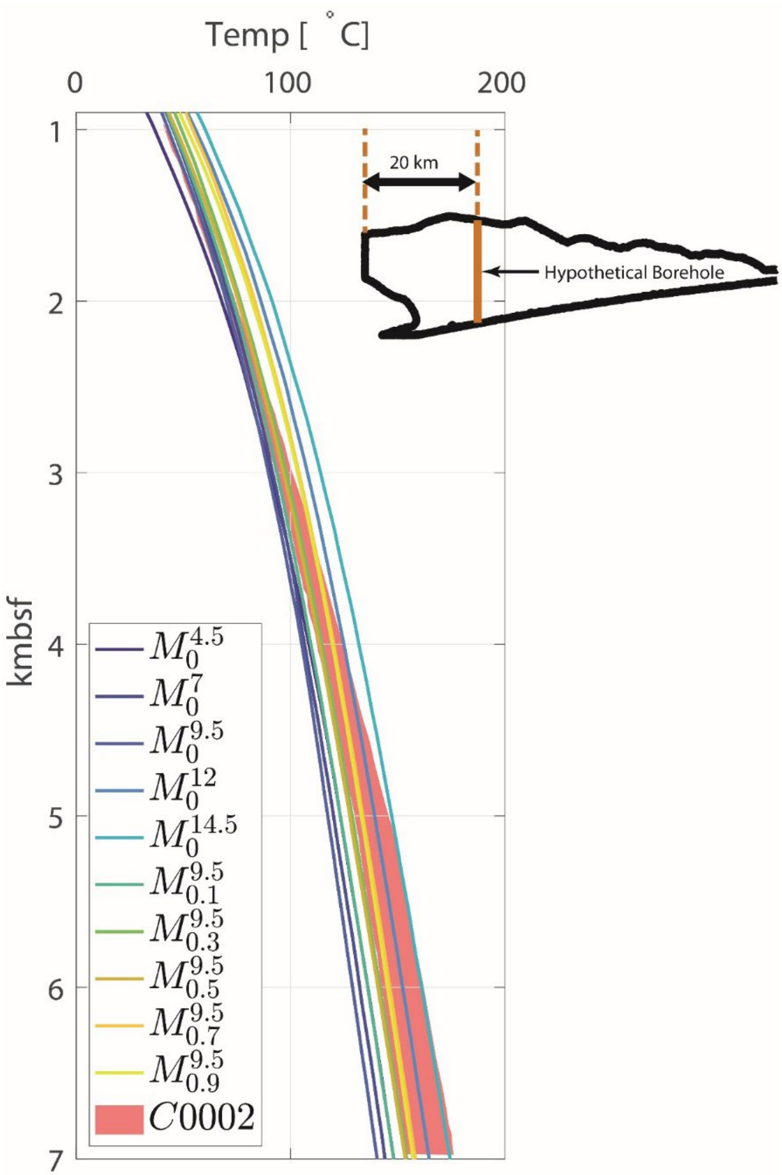

Fig. S15

Trajectory of sediments in model. The wedge on top shows the location of individual boreholes relative to the position of the trench at 2.5 Myr. In each borehole, A-L 10 points are plotted for their trajectories between 2.5 Myr and 7.5 Myr. The color of markers in the trajectories represent the evolution of thermal maturity on individual sediment markers while undergoing evolution. The image of the wedge on top is a representative image showing the relative location of boreholes with respect to the trench and each other. We present 4 set of boreholes (each having 3 boreholes separated by a km), one of which lies in the wedge itself at 2.5 Myr and 3 lies in the incoming sediments as a distance of 1 km, 50km and 100 kms from trench.

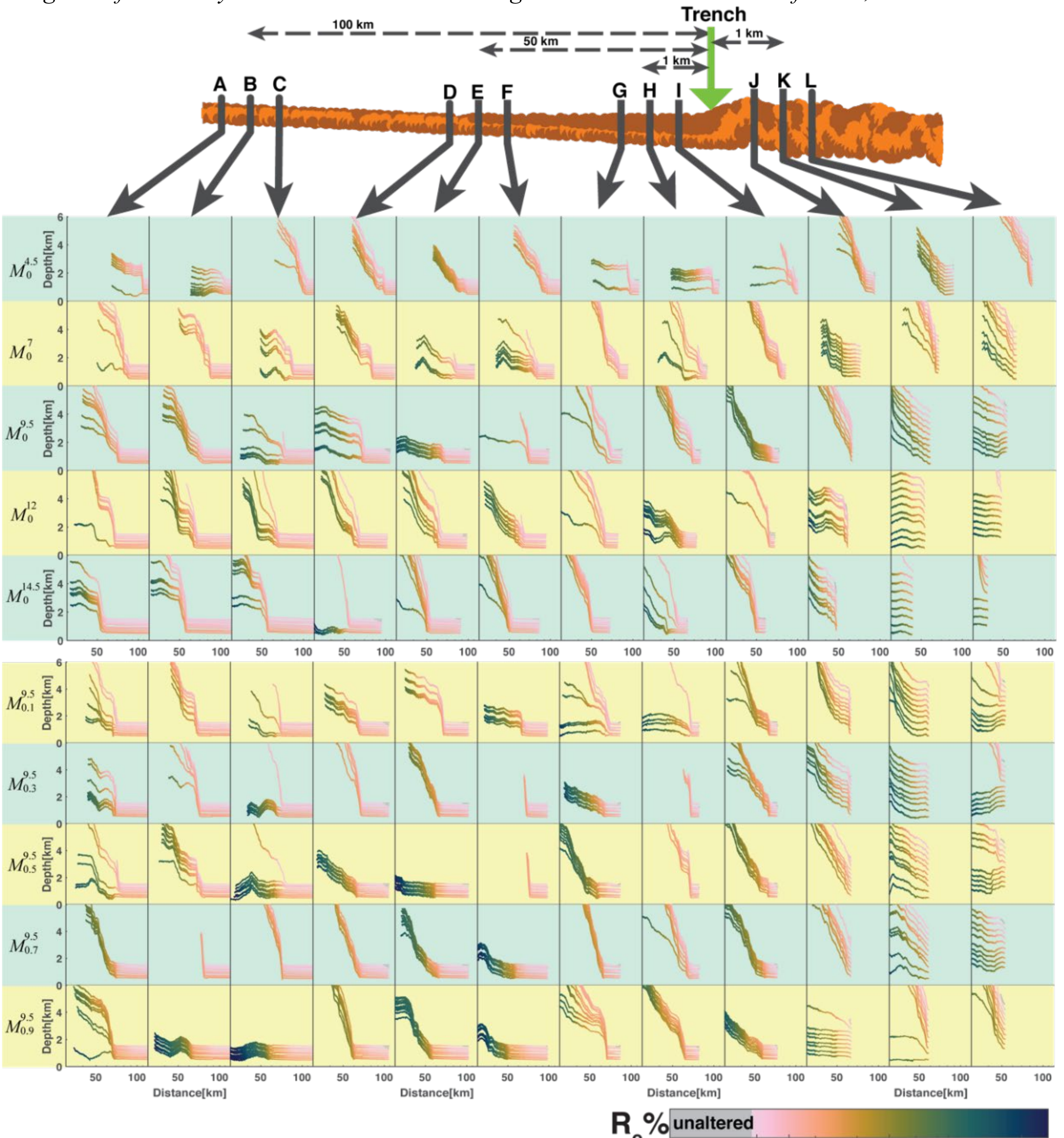

Fig. S16

Vitrinite Reflectance(%R_o) vs Maximum Exposure temperature in models. Panel A, B and C show the Temperatures as a function of %R_o computed from Easy%R_o, Simple%R_o, Basin%R_o for models $\boldsymbol{M_0^{4.5} - M_0^{14.5}}$. *Similarly panels D, E and F show the Temperatures as a function of %R_o computed from Easy%R_o, Simple%R_o, Basin%R_o for models* $\boldsymbol{M_{0.1}^{9.5} - M_{0.9}^{9.5}}$.

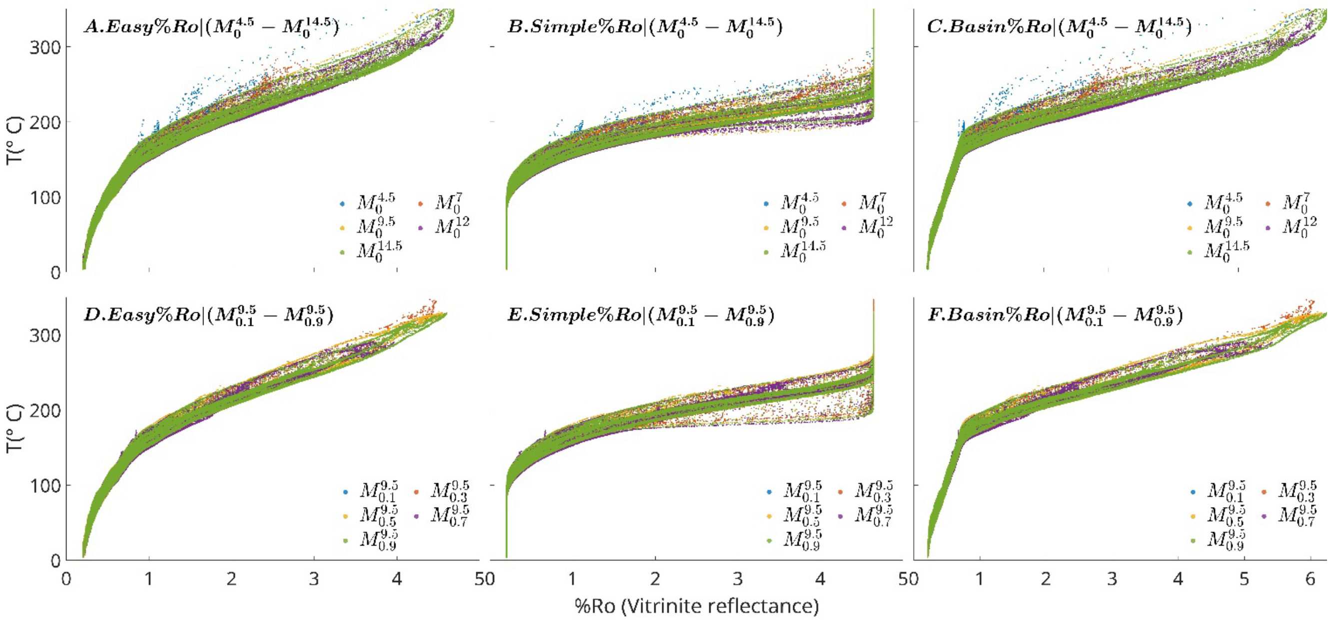

Fig. S17:

Panel A shows %R_o vs T for model (shown by smaller markers) and C0002 borehole (shown by large circular markers) (Fukuchi et al., 2017). Y_n is the depth of the marker from the surface normalized by the thickness (vertical extent) of the wedge at the location of the marker as illustrated in Panel B.

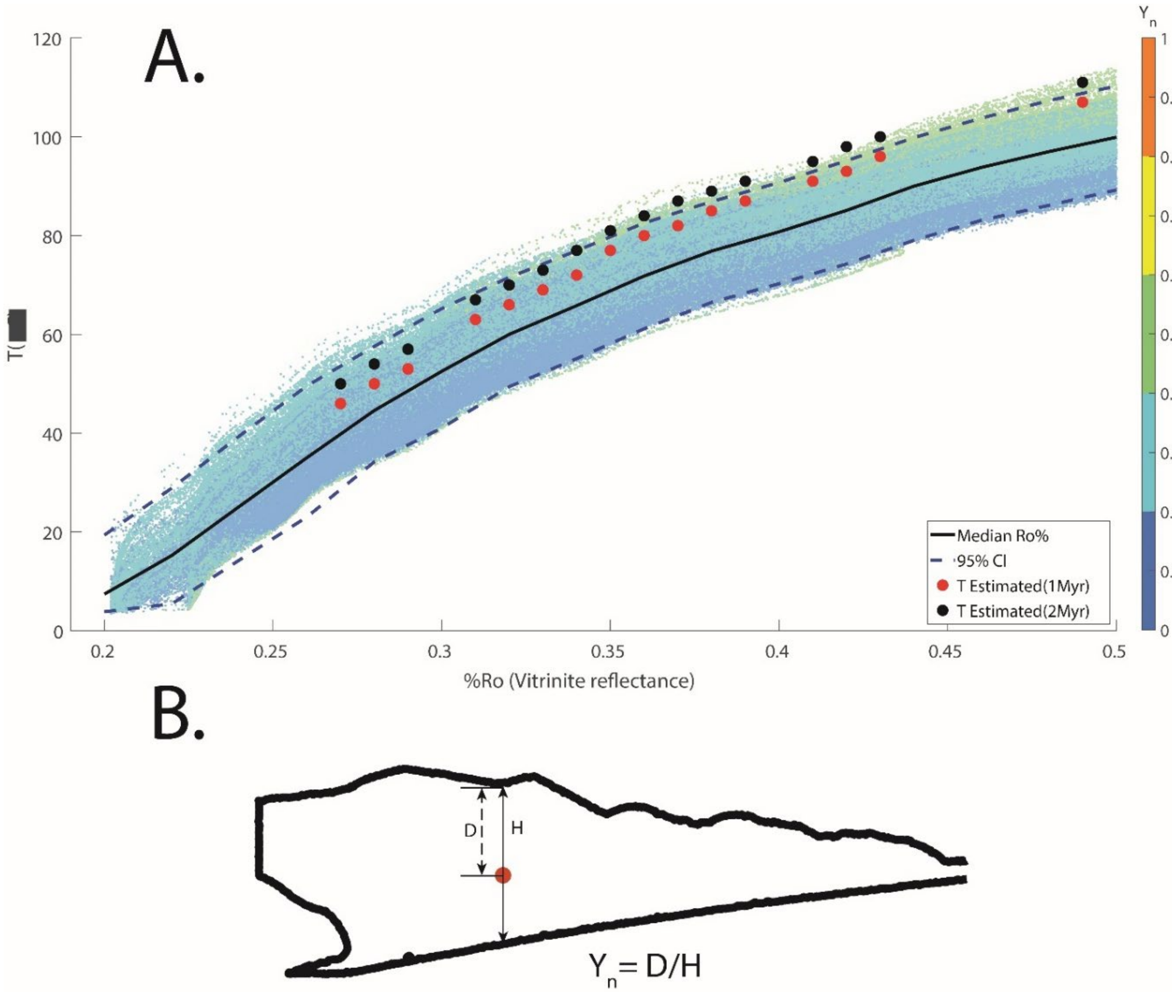

Fig. S18:

Illustration to show the measurement of L (length of wedge), α (surface slope), ***β***(basal dip and, D(Distance between the first and second frontal thrust).

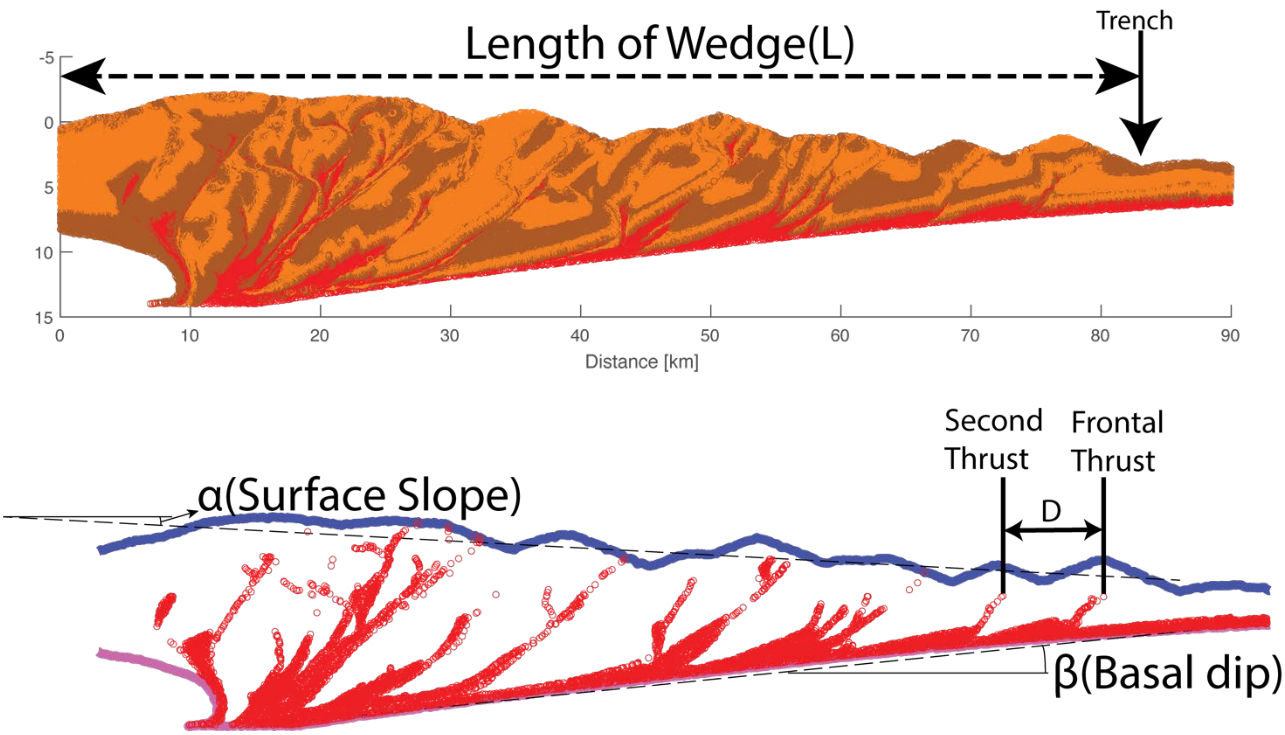

Fig S19:

Evolution of %R_o for constant temperatures with time (computed using Simple %R_o)

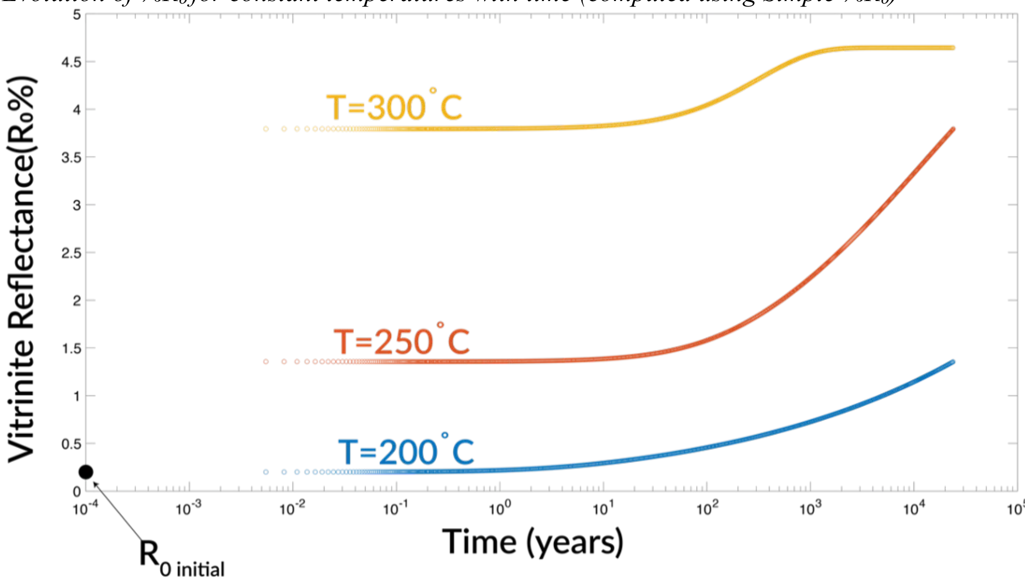

Fig S20:

Thermal maturity distribution in two models with different convergent velocity. Panel A and B shows a models with convergent velocity of 5 cm/yr and 7.5 cm/yr respectively. The colormap for the images is same as for Figure 3. The comparison between the models has been shown for different time to keep the volume of incoming sediments ($T*V_{conv}$) similar.